Two-stage kinetics of field-induced aggregation of medium-sized magnetic nanoparticles

H. Ezzaier, J. Alves Marins, I. Razvin, Micheline Abbas, A. Ben Haj Amara, A. Zubarev, P. Kuzhir

Two-stage kinetics of field-induced aggregation of medium-sized magnetic nanoparticles

H. Ezzaier[1,2], J. Alves Marins[1], I. Razvin[1], M. Abbas[3], A. Ben Haj Amara[2], A. Zubarev[4], and P.Kuzhir[1,*]

[1] *University Côte d'Azur, CNRS UMR 7010 Institute of Physics of Nice, Parc Valrose, Nice 06100, France*

[2]*Laboratory of Physics of Lamellar Materials and Hybrid Nano-Materials, Faculty of Sciences of Bizerte, University of Carthage, 7021 Zarzouna, Tunisia,*

[3]*Laboratoire de Génie Chimique, Université de Toulouse, CNRS-INPT-UPS, Allée Emile Monso, 31030 Toulouse, France*

[4]*Urals Federal University, Department of Mathematical Physics, Lenina Ave 51, 620083 Ekaterinburg, Russia*

Abstract

The present paper is focused on theoretical and experimental study of the kinetics of field-induced aggregation of magnetic nanoparticles of a size range of 20-100 nm. Our results demonstrate that (a) in polydisperse suspensions, the largest particles could play a role of the centers of nucleation for smaller particles during the earliest heterogeneous nucleation stage; (b) an intermediate stage of the aggregate growth (due to diffusion and migration of individual nanoparticles towards the aggregates) is weakly influenced by the magnetic field strength; (c) the stage of direct coalescence of drop-like aggregates (occurring under magnetic attraction between them) plays a dominant role at the intermediate and late stages of the phase separation, with the timescale decreasing as a square of the aggregate magnetization.

I. Introduction

Magnetic micro- and nanoparticles and their liquid suspensions or gels are gaining a growing interest in environmental and biomedical applications, such as water purification from organic and inorganic molecules[1,2], magnetic resonance imaging[3,4], cell separation[5], protein purification[6,7], magnetic hyperthermia[8,9], controlled drug delivery and release[10,11], magneto-mechanical lysis of tumor cells[12,13], high sensitivity immunoassays[14] and tissue engineering[15,16]. In many of these applications, magnetic particles are subject to aggregation induced by an external applied magnetic field, and the kinetics of aggregation becomes an important factor affecting efficiency of a considered system. An excellent example is enhancement of the magnetophoresis of magnetic microbeads due to their field-induced aggregation – the phenomenon referred to as cooperative magnetophoresis[17-20], which could be beneficial for separation and detection of biomolecules using functionalized magnetic microbeads.

Most of existing works characterize the field-induced particle aggregation in terms of three governing parameters – the particle volume fraction ϕ, the ratio of the energy of dipole-dipole interaction between particles to thermal energy – so called dipolar coupling parameter λ and the ratio of the energy of interaction of a magnetic particle with an external magnetic field of an intensity H_0 to thermal energy called magnetic field parameter or Langevin parameter ξ. Both last parameters are defined by the following expressions[21]:

$$\lambda = \frac{m_p^{\,2}}{4\pi\mu_0 k_B T d^3} \propto d^3, \qquad (1a)$$

$$\xi = \frac{m_p H_0}{k_B T} \propto d^3, \qquad (1b)$$

where $\mu_0 = 4\pi\times10^{-7}$ H/m is the magnetic permeability of vacuum; m_p - the particle magnetic moment (in T×m^3); d – its diameter, $k_B \approx 1.38\times10^{-23}$ J/K - the Boltzmann constant and T – absolute temperature. Since the particle magnetic moment is linear with the particle volume, the parameters λ and ξ are proportional to the cube of the particle size. The physics of particle aggregation is rather different for micron-sized particles (with $\lambda>>1$) and for nanoparticles (with $\lambda\sim1$).

Kinetics of field-induced aggregation of micron or sub-micron-sized particles (typically d>100 nm) has been studied experimentally by either direct visualization[22-24] or light scattering[25-28]. The common feature shared between most of the studied systems is that these particles exhibit a rapid field-induced aggregation in linear chains aligned with the direction of applied magnetic field, and the average chain length $\langle 2a \rangle$ grows with time as $\langle 2a \rangle \propto t^{\gamma}$, with $0.45 < \gamma < 0.8$. At longer times, lateral aggregation dominates over tip-to-tip aggregation and the chains can merge and form either a fibrous structure "frozen" in non-equilibrium state likely by inter-particle friction[22] or column structures confined by the walls orthogonal to the applied field[29], or unconfined ellipsoidal drop-like aggregates under pulsed magnetic field[30,31]. Theoretical studies are mainly based on Langevin dynamics simulations[19,32,33] or solution of Smoluchowsky kinetic equation [23,24,27,28,33-35]. A simplified theoretical approach, so-called hierarchical model, has been developed by See and Doi[36] considering only coalescence of the chains of equal sizes and showing a satisfactory agreement with experiments on $\langle 2a \rangle$, even though it predicts monodisperse particle chains instead of experimentally observed polydisperse distribution.

In the opposite size limit, typically d<20 nm, when considering aggregation, one usually speaks about field-induced phase separation or a condensation phase transition. Appropriate phase diagrams and equilibrium microstructures have been extensively studied theoretically and experimentally[37-47]. Kinetics of phase separation has been studied by light scattering by Socoliuc and Bica[48] for aqueous dispersions of nanoparticles (ferrofluids) and by Laskar *et al.*[49] for non-aqueous ferrofluids. Elongated scattered patterns have been reported by these authors corresponding to formation of long drop-like aggregates, which during time settle to a stable space configuration owing to magnetic lateral repulsion. Thermodynamic approach broadly used for molecular liquids is appropriate for modeling of the phase separation in suspensions of magnetic nanoparticles. Using this approach, Zubarev and Ivanov[50] and Ivanov and Zubarev[51] have considered three different stages of the phase separation: (a) appearance of critical nuclei at early stage of homogeneous nucleation; (b) evolution of the nuclei to long drop-like aggregates, and (c) Oswald ripening when the particles are transferred from smaller to larger aggregates leading at infinite times to a full coalescence of the concentrated phase into a single bulk phase. The aggregate size distribution has been calculated and the average aggregate volume has been

found to increase with time as $\langle V \rangle \propto t^{7/4}$ at early stage, followed by an intermediate plateau at the end of the stage (b) showing a final increase with $\langle V \rangle \propto t^{7/6}$ at the ripening stage (c).

Magnetic nanoparticles of medium size, 20<*d*<100 nm have not been available for a long time because of difficulties related to their colloidal stabilization. To prevent their aggregation by magnetic interactions in zero field, they have to be superparamagnetic. So, these particles are usually porous nanoclusters composed of smaller 10-nm superparamagnetic nanoparticles[52-56]. Similarly to small nanoparticles, medium-sized colloids exhibit condensation phase transitions[54,55,57] which enhance drastically their magnetic separation on magnetized collectors[57-61]. Kinetics of phase separation of medium-sized nanoparticles has been studied only scarcely. Socoliuc *et al.*[54] has conducted direct visualization and light scattering experiments on 80-nm magnetic nanoclusters and shown appearance of elongated drop-like aggregates. In addition to three kinetic stages postulated by Zubarev and Ivanov[50] and Ivanov and Zubarev[51], Socoliuc *et al.*[54] claims a forth final stage of coalescence of aggregates into larger domains. This kinetics seems to combine features of condensation phase transitions of small nanoparticles with aggregation of large micron- or submicron-sized particles. To the best of our knowledge, theoretical description of such kinetics is still missing.

The present paper is focused on theoretical modeling of kinetics of aggregation (or phase separation) of the medium-sized (20<*d*<100 nm) superparamagnetic nanoparticles. The main goal is to establish theoretical correlations for the temporal evolution of the aggregate size and shape as function of the initial supersaturation of the suspension (or initial particle volume fraction ϕ_0) and of the applied magnetic field. To check our model, aggregation process is visualized using an optical microscope and the size and shape of the aggregates is analyzed as function of time. Visualization experiments allow assessing dominant mechanisms of aggregation, which are implemented into the theory. Therefore, the present theory is developed for two stages that are explicitly distinguished in our experiments and are interesting from the practical point of view: (a) intermediate aggregate growth by particle diffusion and magnetophoresis, and (b) aggregate coalescence due to dipolar interactions. Simple hierarchical model of See and Doi[36] developed for chain-like clusters is extended to coalescence of drop-like aggregates, while the transition between two aggregation stages is managed by comparison of the aggregation rates at each stage.

The present paper is organized as follows. Theoretical model implying two observed aggregation stages is developed in Sec. II. The aggregate growth and coalescence stages are described in Secs. II-A and II-B, respectively, while the transition between stages is considered in Sec. II-C. Experimental details of optical visualization and image processing are provided in Sec. III. Experimental data on temporal evolution of the aggregate size are compared with theoretical results in Sec. IV, while the conclusions and perspectives are outlined in Sec. V.

II. Theory

A. Aggregate growth

Let us consider initially homogeneous suspension of Brownian super-paramagnetic hard sphere particles, all having the same diameter *d*, and dispersed at a volume fraction φ_0 in a Newtonian liquid of a dynamic viscosity η_0. In the absence of any external magnetic field, the

particles magnetic moment is zero, they do not exhibit dipolar interactions and do not form any clusters.

When a uniform external magnetic field, of intensity H_0, is applied, particles acquire magnetic moments and attract to each other, while the Brownian motion tends to re-disperse them. Depending on the values of φ_0 and H_0, the suspension undergoes a phase separation manifested by appearance of elongated aggregates. At infinite times the systems tends to a thermodynamic equilibrium at which the particle volume fraction in the dilute (outside the aggregates) and concentrated (inside the aggregates) phases tend to steady-state values φ' and φ'' depending on H_0, while $\varphi'(H_0)$ and $\varphi''(H_0)$ dependences correspond to coexistence curves of a H_0-φ phase diagram[38]. Such diagrams have been modeled for our particular nanocluster suspensions[55,57], and strong inequality $\varphi'' >> \varphi'$ has been found. In the present paper, φ' is directly measured as function of H_0 [see figure 6 in Sec. IV-A], while the value φ''~0.6 close to the random close packing limit is taken for the aggregates. In this section, we intend to find the evolution of the aggregate size and shape with time and as a function of two governing dimensionless parameters $\Delta_0 = \varphi_0 - \varphi'$ called initial supersaturation[62] and ξ - the magnetic field parameter depending on H_0 [Eqs. (1b), (10)].

The aggregation starts by a short nucleation stage not considered here, which is most likely heterogeneous and during which primary aggregates composed of large number of particles are expected to appear around the biggest particles playing a role of nucleation centers. These primary aggregates are supposed to be of the same size and to have a shape modeled by a prolate ellipsoid of revolution extended along the applied magnetic field as commonly admitted in theoretical models[30,50,51] and observed in experiments with ferrofluids[48,54,63-65]. Initial volume V_0 and initial volume fraction Φ_0 of primary aggregates (ratio of the total volume of all the aggregates to the suspension volume) are considered as adjustable parameters of the model.

During time, individual magnetic particles of the dilute phase surrounding the aggregates are attracted to the aggregates and induce the aggregate growth. The aggregates are supposed to conserve their ellipsoidal shape but their concentration Φ in the suspension and size, characterized by a major semi-axis a, a minor semi-axis b (as depicted in Fig. 1) and a volume $V = 4\pi ab^2/3$, increase progressively with time. Nevertheless, the aggregate concentration is supposed to remain low enough $\Phi<<1$ (approximation valid for very dilute suspensions with $\Delta_0/\varphi'' << 1$), and possible coalescence of aggregates at this stage is neglected. The aggregate shape is quantified by their aspect ratio $r_a=a/b$, which is assumed to be very high, $r_a>>1$, in agreement with numerous observations[48,54,63-65]. During all this aggregation stage, the aggregates are supposed to be of equal size, their number concentration is assumed to be constant with time $n = \Phi/V = \Phi_0/V_0$, while possible appearance of new nuclei is neglected. These rough approximations are to some extent supported by the more precise theory of aggregation of small nanoparticles[50] (d<20 nm).

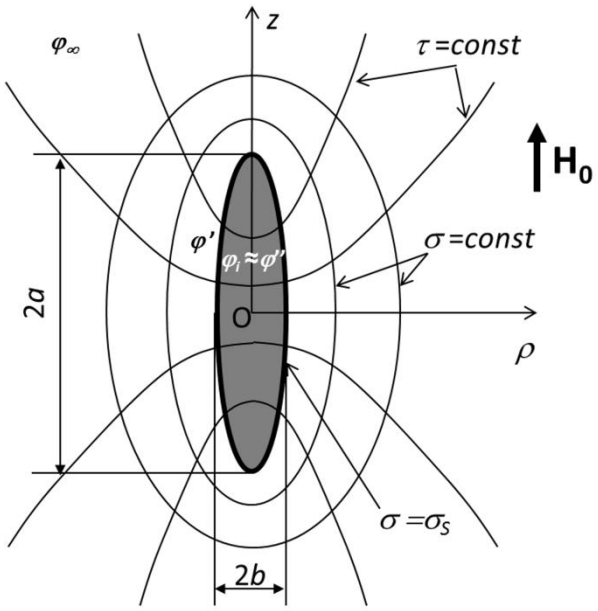

Fig.1. Sketch of the ellipsoidal aggregate. Cylindrical and ellipsoidal coordinates are introduced. Key values of the particle concentration inside the aggregate (φ"), on the outer side of the aggregate surface (φ') and far from the aggregate (φ_∞) are also indicated. The external uniform magnetic field $\mathbf{H}_0$ is oriented along the z-axis.

The internal aggregate volume fraction φ_i (ratio of volumes of all particles constituting the aggregate to the aggregate volume) is supposed to be close to the equilibrium concentration of the concentrated phase: $\varphi_i \approx \varphi$"~0.6, while the particle concentration in any point of the dilute phase around the aggregate is $\varphi << \varphi_i$. Finally, possible sedimentation of individual particles and aggregates is neglected. This assumption is justified in Sec. III.

The starting point of the model is the particle conservation equation implying that the growth rate, dN/dt of the number of particles, N, in the aggregate is equal to the particle flux J towards the aggregate:

$$J = \frac{dN}{dt} = \frac{(n_i - n_s)dV}{dt} \approx \frac{\varphi"}{v}\frac{dV}{dt}, \qquad (2)$$

where $n_i = \varphi_i / v \approx \varphi"/v$ is the number concentration of particles inside the aggregates; $n_s = \varphi_s / v$ and φ_s are respectively the number concentration and the volume concentration of individual particles around the aggregate in the vicinity of its surface; v is the volume of primary particles.

The particle flux density **j** outside the aggregates at any point of the dilute phase is related to the gradient of the local chemical potential μ and local volume fraction φ of particles. The expressions for μ and **j** take the following form in the dilute-limit approximation[50,66]:

$$\mu = k_B T \ln\varphi + U = k_B T \ln\left(\varphi e^{u}\right), \qquad (3a)$$

$$\mathbf{j} = -\zeta\frac{\varphi}{v}\nabla\mu = -\frac{D}{v}e^{-u}\nabla\left(\varphi e^{u}\right), \qquad (3b)$$

where ζ and $D=\zeta k_B T=k_B T/(3\pi\eta_0 d)$ are the particle mobility and diffusion coefficient, respectively; U and $u=U/(k_B T)$ are respectively the dimensional and dimensionless energies of magnetic interaction of a particle with the local field H at a given position of the particle outside the aggregate. The expression for U takes the following form under the approximation of linear magnetization of particles, valid at low magnetic field intensities $H_0 \le 4$ kA/m, considered in our experiments[67]:

$$U=-\int m_p dH \approx -\frac{3}{2}\mu_0\beta_p H^2 v, \qquad (4)$$

where $\beta_p=\chi_p/(3+\chi_p)$ is the magnetic contrast factor of an individual nanoparticle of a magnetic susceptibility χ_p. The spatial distribution of the magnetic field H around the ellipsoidal aggregate and the dimensionless energy u are calculated in Appendix A.

Let us introduce axisymmetric ellipsoidal coordinate system (σ, ϕ, τ), with an origin situated at the aggregate center and whose coordinate surfaces σ=const and τ=const represent confocal ellipsoids of revolution and hyperboloids of revolution, respectively [Fig. 1]. These coordinates are related to the coordinates (ρ, ϕ, z) of the cylindrical coordinate system by the following expressions[68]:

$$z=c\sigma\tau; \qquad \rho^2=c^2(\sigma^2-1)(1-\tau^2); \qquad \sigma\ge\sigma_s>1; \qquad -1\le\tau\le 1, \qquad (5)$$

where $c^2=a^2-b^2$ and $\sigma_s=a/c$ is the value of σ on the aggregate surface. The polar coordinate ϕ is common for both coordinate systems. The metric coefficients of the ellipsoidal system are

$$g_{\sigma\sigma}=c^2\frac{\sigma^2-\tau^2}{\sigma^2-1}; \qquad g_{\tau\tau}=c^2\frac{\sigma^2-\tau^2}{1-\tau^2}; \qquad g_{\phi\phi}=c^2(\sigma^2-1)(1-\tau^2). \qquad (6)$$

The particle diffusion towards the aggregates is considered in quasi-stationary approximation $\mathrm{div}\,\mathbf{j}\approx 0$, for which it can be shown that (a) the particle flux J through the surfaces σ=*const* is independent of σ; (b) the chemical potential of particles outside the aggregates depends only on the coordinate σ, and (c) the product φe^u intervening into Eq. (3b) is independent of τ. Bearing this in mind, we arrive at the following expressions for the normal component of the particle flux density and the flux through a coordinate surface σ=*const*:

$$j_\sigma=-\frac{D}{v}e^{-u}\frac{1}{\sqrt{g_{\sigma\sigma}}}\frac{\partial}{\partial\sigma}\left(\varphi e^u\right), \qquad (7a)$$

$$J=-\oint j_\sigma dS=-\int_0^{2\pi}\int_{-1}^{1} j_\sigma\sqrt{g_{\tau\tau}g_{\phi\phi}}\,d\tau d\phi=2\pi\frac{D}{v}c(\sigma^2-1)\frac{\partial}{\partial\sigma}\left(\varphi e^u\right)\int_{-1}^{1}e^{-u}d\tau, \qquad (7b)$$

where we make use of Eq. (6) for the metric factors and the minus sign in Eq. (7b) comes from the fact that the particle flux is the oriented towards the aggregate. Isolating the term $\partial\left(\varphi e^u\right)/\partial\sigma$, and integrating over σ from σ_s to infinity, we get the following expression for the particle flux independent of the coordinate σ:

$$J = 2\pi \frac{D}{v} c \frac{\varphi_\infty e^{u_0} - \varphi_s e^{u_s}}{\int_{\sigma_S}^{\infty} \left[(\sigma^2 - 1) \int_{-1}^{1} e^{-u} d\tau \right]^{-1} d\sigma}. \quad (8)$$

Here u_0 is the dimensionless energy of the particle in the external filed H_0, φ_∞ is the particle volume fraction at the infinite distance from the aggregate, u_s and φ_s are respectively the dimensionless energy and concentration of particles at any point (σ_s, τ) situated on the outer side of the aggregate surface. Since the product $\varphi_s e^{u_s}$ is independent of τ, it can be replaced by $\varphi_{s0} e^{u_0}$, where φ_{s0} is the particle concentration at the point of the aggregate surface where the magnetic field intensity is equal to H_0. Furthermore, the local thermodynamic equilibrium at the aggregate surface imposes that the concentration outside and inside the aggregate are approximately equal to the binodal concentrations: $\varphi_{s0} \approx \varphi'$ and $\varphi_i \approx \varphi''$ [Fig. 1]. This allows expressing the particle flux through the supersaturation $\Delta = \varphi_\infty - \varphi'$ of the suspension:

$$J = 2\pi \frac{D}{v} c \frac{\Delta}{I}, \quad (9)$$

where the integral $I = \int_{\sigma_S}^{\infty} \left[(\sigma^2 - 1) \int_{-1}^{1} e^{-(u-u_0)} d\tau \right]^{-1} d\sigma$ is estimated in Appendix B [cf. Eq. (B-6)] as a function of the magnetic field parameter [Eq. (1b)], which, for the case of the medium-sized magnetic nanoparticles with induced dipole moment and linear magnetization appears to be proportional to the square of the magnetic field intensity H_0 and takes the following form:

$$\xi = -u_0 = \frac{3\mu_0 \beta_p H_0^2 v}{2k_B T}. \quad (10)$$

In the aforementioned case, the parameter ξ is closely related to the dipolar coupling parameter λ [Eq. (1a)] through: $\xi = \beta_p \lambda / 4$. In the considered limit of high aspect ratio aggregates, $r_a = a/b >> 1$, the magnitude c intervening into Eq. (9) could be expressed through the aggregate volume $V = 4\pi a b^2 / 3$:

$$c = (a^2 - b^2)^{1/2} \approx a = \left(\frac{3}{4\pi} V r_a^2 \right)^{1/3}. \quad (11)$$

On the other hand, the local thermodynamic equilibrium of an aggregate requires the minimization of its free energy at any time and leads to the following key relationship[50] between the aggregate volume V and its aspect ratio r_a valid at $r_a >> 1$:

$$V \approx B \frac{r_a^7}{\ln^3 r_a}; \quad B = \frac{\pi^4}{48} \left(\frac{\Sigma}{\mu_0 M^2} \right)^3, \quad (12)$$

where M is the aggregate magnetization and Σ – the aggregate surface tension. The volume-scale B has been shown to be of the order of particle volume[69]: $B \sim \pi^3 v / 64$. Equation (12) allows expressing $\ln r_a$ and r_a through V using the strong inequality $\ln(\ln r_a) << \ln r_a$ valid at $r_a >> 1$:

$$\ln r_a \approx \frac{1}{7}\ln\frac{V}{B}, \tag{13a}$$

$$r_a = \left(\frac{V}{B}\right)^{1/7} \ln^{3/7} r_a \approx \left(\frac{V}{B}\right)^{1/7} \left(\frac{1}{7}\ln\frac{V}{B}\right)^{3/7}. \tag{13b}$$

Combining together Eqs. (2), (9), (11), (13) and (B-6), equation (2) of the aggregate growth takes the following form:

$$\varphi''\frac{dV}{dt} \approx \frac{4\pi\kappa}{K} DB^{1/3} \frac{(V/B)^{3/7}}{\ln^{5/7}(V/B)}\Delta, \tag{14}$$

where $\kappa = 7^{5/7}(4\pi/3)^{-1/3} \approx 2.5$ and K is a numerical factor depending on ξ and given by Eq. (B-6b) in Appendix B.

To integrate Eq. (14), we need to relate the supersaturation $\Delta = \varphi_\infty - \varphi'$ to the aggregate volume V. First, the concentration φ_∞ can be estimated from the condition of conservation of the total volume of particles in the suspension:

$$\varphi_0 = \Phi\varphi_i + (1-\Phi)\varphi_\infty, \tag{15}$$

with $\varphi_i \approx \varphi''$. Second, under the aforementioned assumption of a constant number of aggregates during the aggregate growth stage, ($n = \Phi/V \approx const = \Phi_0/V_0$), the aggregate concentration Φ at a given time t is related to the aggregate initial volume V_0 and concentration Φ_0 by

$$\Phi \approx \Phi_0 \frac{V}{V_0}. \tag{16}$$

Combining Eqs. (15) and (16), and taking into account the smallness of the aggregate concentration, Φ<<1, in initially dilute suspension with φ_0<<1, we obtain:

$$\Delta = \varphi_\infty - \varphi' = \frac{\varphi_0 - \varphi''\Phi}{1-\Phi} - \varphi' \approx \Delta_0 - \varphi''\Phi_0\frac{V}{V_0}. \tag{17}$$

Recall that $\Delta_0 = \varphi_0 - \varphi'$ is the initial supersaturation. The time integration of Eq. (14) with the initial condition $V(0)=V_0$ leads to the following expression for the elapsed time t as function of the dimensionless volumes $\hat{V} = V/B$ and $\hat{V}_0 = V_0/B$:

$$t = \frac{K\varphi''}{4\pi\kappa}\left(\frac{B^{2/3}}{D}\right)\int_{\hat{V}_0}^{\hat{V}}\left[\frac{\hat{V}^{3/7}}{(\ln\hat{V})^{5/7}}\left(\Delta_0 - \varphi''\Phi_0\frac{\hat{V}}{\hat{V}_0}\right)\right]^{-1} d\hat{V}. \tag{18}$$

One can fit Eq. (18) by the following formula, exact at both short and long time limits:

$$t \approx \frac{K}{4\pi\kappa}\left(\frac{B^{2/3}}{D}\right)\frac{\hat{V}_0}{\Phi_0}\frac{(\ln\hat{V})^{5/7}}{\hat{V}^{3/7}} f\left(\frac{\Delta}{\Delta_I}\right)\ln\frac{\Delta_I}{\Delta}, \tag{19-a}$$

$$f\left(\frac{\Delta}{\Delta_I}\right)=1+0.8\left(\frac{\Delta}{\Delta_I}\right)^{0.45}\left(1-\frac{\Delta}{\Delta_I}\right)^{0.3}, \qquad \text{(19-b)}$$

where $\Delta_I=\Delta_0-\varphi''\Phi_0$ is the suspension supersaturation at the beginning of the aggregate growth stage corresponding to primary aggregates with a volume V_0. Both theoretical dependencies (18) and (19) of the dimensionless volume $\hat{V}=V/B$ on the dimensionless time $\hat{t}=Dt/B^{2/3}$ are plotted in Fig. 2 for the following values of the parameters appropriate for our experimental conditions: $\Delta_0=10^{-4}$, $\Phi_0=10^{-6}$, $\varphi''=0.6$, $\hat{V}_0=10^7$, $K=1$.

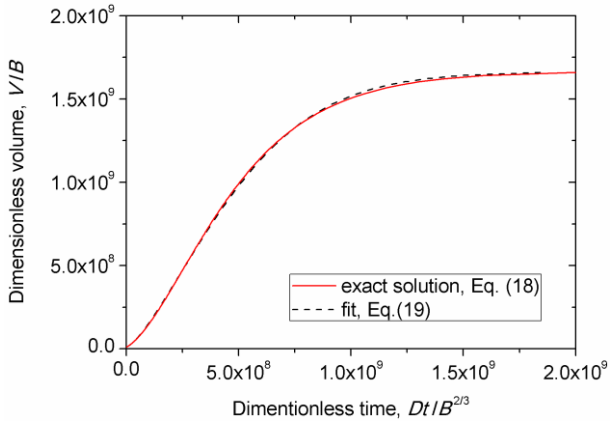

Fig. 2. Theoretical dependence of the dimensionless aggregate volume on the dimensionless time for the aggregate growth stage. The following set of parameters were used in calculations: $\Delta_0=10^{-4}$, $\Phi_0=10^{-6}$, $\varphi''=0.6$, $\hat{V}_0=10^7$, $K=1$.

The aggregate volume exhibits an initial sharp increase with time and becomes almost constant at longer times. Such saturation of the aggregate volume corresponds to the vanishing of the suspension supersaturation Δ [Eq. (17)] with time when the dilute phase concentration φ_∞ approaches the binodal concentration φ' and the aggregate concentration tends to its maximum value dictated by particle conservation [Eq. (15)]: $\Phi_m\approx\Delta_0/\varphi''<<1$. However, such a state with a final number of aggregates, $n\approx\Phi_0/V_0$, is thermodynamically unfavorable, since aggregates start to coalesce in order to decrease the suspension free energy – the mechanism considered in Sec. II-B. Another striking point is that the characteristic time of the aggregate growth is about nine orders of magnitude higher than the diffusion timescale $t\sim B^{2/3}/D\sim d^2/D$ at the considered set of parameters. This is explained by the fact that the aggregates contain a very large number of particles (10^7-10^9 in the current example), and the real time scale is based on the aggregate volume, rather than on the particle volume, as inferred from Eq. (19): $t\sim(B^{2/3}/D)(\hat{V}_m^{4/7}/\Delta_0)$.

Finally, the considered kinetics includes both diffusive and magnetophoretic particle fluxes related respectively to the 1st and the 2nd term of Eq. (3a) for the chemical potential. The diffusive flux arises thanks to the fact that the particle concentration in the dilute phase in the vicinity of the aggregate surface is close to the equilibrium value φ' and is lower than the concentration φ_∞ far from the aggregate. The magnetophoretic flux is responsible for particle

migration towards the aggregate due to magnetic attraction. The contribution of magnetophoretic flux appears in final equations (18) and (19) through the numerical multiplier $K \leq 1$, which is logarithmically decreasing function of the magnetic field parameter ξ [cf. Eq. (B-6b) in Appendix B]. The magnetophoretic flux (or the value of K) does not change the shape of the time dependency of the aggregate volume [Fig. 2] but decreases the time of the aggregate growth, with respect to the time governed exclusively by diffusive flux.

B. Aggregate coalescence

As already pointed out, the state with a finite number of aggregates is thermodynamically unfavorable, the system tends to decrease the surface area between concentrated and dilute phases, which promotes coalescence of aggregates, even if their concentration is low. In the present section, we consider the coalescence stage of the phase separation neglecting possible aggregate growth by absorption of individual particles from the dilute phase. This assumption is valid if the timescale of the aggregate growth stage is much shorter than that of the coalescence stage, such that the dilute phase concentration φ_∞ rapidly approaches the binodal concentration φ' and the aggregates no more able to absorb particles from the surrounding fluid. The coalescence is supposed to begin when the aggregates achieve some initial volume V_τ, same for all of them, and initial volume fraction Φ_τ, which can be different from those used for the initial conditions of the aggregate growth stage [Sec. II-A]. Again, during all this stage, the aggregates are assumed to preserve their ellipsoidal shape, high aspect ratio r_a>>1, low concentration Φ<<1 and to be of the same size. We seek for the evolution of the aggregate volume with time thanks to their coalescence induced by magnetic attraction between them.

To this purpose, we adopt the basic idea of the hierarchical model of See and Doi[36], who considered that all pairs of primary aggregates coalesce at the same time producing secondary aggregates of a volume $2V_\tau$, then, all the pairs of secondary aggregates coalesce at the same time into the aggregates of a volume $4V_\tau$, and so on, until full coalescence of the bulk concentrated phase. At the beginning of the coalescence stage (t=0), the initial number fraction of aggregates is $n_\tau = \Phi_\tau / V_\tau$. Let τ_0 be the time for two neighboring aggregates to coalesce into an aggregate of a volume $V_1 = 2V_\tau$. The number concentration of the aggregates at $t = \tau_0$ is divided by two, $n_1 = n_\tau / 2$, while the volume fraction does not change, $\Phi_1 = \Phi_\tau$ under considered assumption that the aggregate do not absorb individual particles from the surrounding fluid. After the first coalescence, the secondary aggregates will coalesce into aggregates of a volume $V_2 = 2V_1 = 2^2 V_\tau$ at number fraction $n_2 = n_\tau / 2^2$ during a time interval τ_1. The i-th coalescence step will correspond to the aggregate volume $V_k = 2^k V_\tau$, the number fraction $n_k = n_\tau / 2^k$ and the volume fraction $\Phi_k = \Phi_\tau \equiv \Phi$, while the total elapsed time from the beginning of the process is $t_k = \sum_{i=0}^{k-1} \tau_i$. We have now to relate the time interval τ_i of each i-th coalescence step to the aggregate volume V_i.

To this purpose, let us consider two identical drop-like aggregates aligned with the applied magnetic field and having a major semi-axis a, a minor semi-axis b, an aspect ratio $r_a = a/b$>>1 and a volume $V = 4\pi ab^2/3$. Mutual position of their centers is described by a

distance r and an angle θ in a spherical coordinate system with an origin in the center of the first aggregate [Fig. 3a]. The average position (r, θ) of a pair of aggregates should meet the requirement of the volume conservation of the concentrated phase, which can be satisfied by a cell model often used in mechanics and optics of composite materials[70,71]. Each aggregate is supposed to be situated inside an ellipsoidal cell having an aspect ratio r_a equal to that of the aggregate and a volume equal to V/Φ. The major and minor semi-axes of the cell are equal to $a/\Phi^{1/3}$ and $b/\Phi^{1/3}$, respectively. From geometrical considerations, the center of the second aggregate can be situated at any point on the surface of a control ellipsoid [dotted line on Fig. 3a] with semi-axes $\alpha = 2a/\Phi^{1/3}$ and $\beta = 2b/\Phi^{1/3}$. The time interval of a given coalescence step can be evaluated as inverse of the aggregate flux through the surface of this ellipsoid.

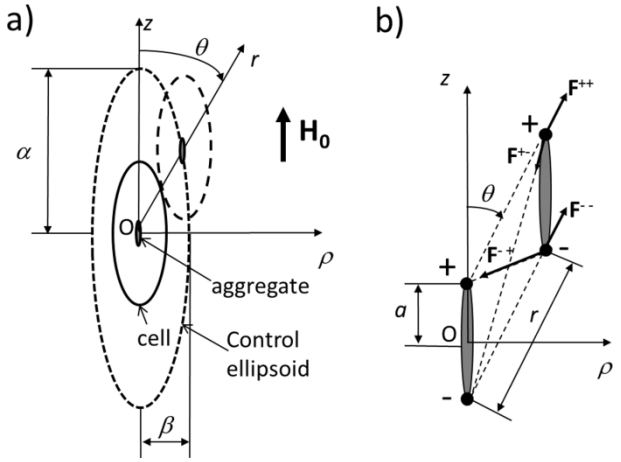

Fig. 3. Sketches of the cell model (a) and of the "four charges" model (b). In both cases, the external uniform magnetic field $\mathbf{H}_0$ is oriented along the z-axis

During the coalescence stage, the aggregates have a size of several microns and their diffusive flux is therefore negligible. The magnetophoretic flux of the aggregates through the surface of the control ellipsoid is expressed through the force $\mathbf{F}$ of magnetic interactions between two aggregates as follows:

$$J = -2\int_{J>0} n(\boldsymbol{\zeta}\cdot\mathbf{F})\cdot\mathbf{n}dS = -\left(2n\zeta_{\perp}\int_{J>0} F_{\rho}n_{\rho}dS + 2n\zeta_{\text{II}}\int_{J>0} F_z n_z dS\right), \qquad (20)$$

where $n = \Phi/V$ is the aggregate number fraction supposed to be homogeneous on the aggregate surface; $\mathbf{n}$ is the outward unit vector normal to the control ellipsoid surface; $\zeta_{\perp}, \zeta_{\text{II}}$ are the transverse and longitudinal diagonal components of the aggregate mobility tensor $\boldsymbol{\zeta}$. The two terms in the right-hand side of Eq. (20) correspond to the radial and axial components of the flux with respect to the cylindrical coordinate system (ρ, ϕ, z) introduced in Fig. 3a. The factor 2 before the integrals comes from the fact that both aggregates are moving towards each other at the same speeds, while the minus sign stands for the positive inward flux. The integration domain $J>0$ corresponds to the fact that only inward flux is considered to contribute to the coalescence of a given pair of aggregates, while the outward flux would induce a coalescence of another pair. The products $n_{\rho}dS$ and $n_z dS$ are the projections of the surface element dS on the z-φ and r-φ coordinate surfaces, respectively. They have the following expression in cylindrical coordinates: $n_{\rho}dS = 2\pi\rho(z)dz$ and $n_z dS = 2\pi\rho d\rho$, where $\rho(z) = (\alpha^2 - z^2)^{1/2}/r_a$ on the control ellipsoid surface. The expression (20) for the flux reads:

$$J = -2\left(4\pi n\zeta_{\perp} \int_{z_0}^{\alpha} F_{\rho}\rho(z)dz + 4\pi n\zeta_{\text{II}} \int_{0}^{\rho_0} F_z \rho d\rho \right), \qquad (21)$$

where (ρ_0, z_0) are the coordinates of the point on the control ellipsoid surface where the flux density is zero.

The magnetic force **F** will be estimated in a "four charges" approximation initially developed for chains of magnetic particles[29]. By analogy with electrostatics, the induced dipole moment of each aggregate is supposed to be a result of two opposite point charges q and $-q$ concentrated at the aggregate tips, as shown schematically in Fig. 3b. The charge q is related to the aggregate dipole moment $m_a = 2aq$, and the latter is defined though the aggregate magnetization M as $m_a = \mu_0 MV$, such that $q = \mu_0 MV/(2a)$. Absolute values of the four forces acting on the poles of the right aggregate in Fig. 3b are given by the Coulomb's law, neglecting magnetic susceptibility of the medium surrounding the aggregates:

$$F^{++} = F^{--} = \frac{q^2}{4\pi\mu_0 r^2}; \qquad F^{+-} = \frac{q^2}{4\pi\mu_0 r_1^{\,2}}; \qquad F^{-+} = \frac{q^2}{4\pi\mu_0 r_2^{\,2}}, \qquad (22)$$

where $r^2 = \rho^2 + z^2$, $r_1^{\,2} = \rho^2 + z_1^{\,2}$ and $r_2^{\,2} = \rho^2 + z_2^{\,2}$ are the squares of the distances between different pairs of charges belonging to two aggregates; r corresponds to the distance between the centers of two aggregates; $z_1 = z + 2a$ and $z_2 = z - 2a$. The radial and axial components of the total force acting on the right aggregate of Fig. 3 read:

$$F_{\rho} = (F^{++} + F^{--})\sin\theta - F^{+-}\sin\theta_1 - F^{-+}\sin\theta_2 = \frac{q^2}{4\pi\mu_0}\left(\frac{2}{r^3} - \frac{1}{r_1^3} - \frac{1}{r_2^3}\right)\rho; \qquad (23\text{-a})$$

$$F_z = (F^{++} + F^{--})\cos\theta - F^{+-}\cos\theta_1 - F^{-+}\cos\theta_2 = \frac{q^2}{4\pi\mu_0}\left(\frac{2z}{r^3} - \frac{z_1}{r_1^3} - \frac{z_2}{r_2^3}\right), \qquad (23\text{-b})$$

Where θ, θ_1 and θ_2 are the angles between the z-axis and the lines connecting different pairs of charges belonging to two aggregates; θ corresponds to the angle that the line connecting the aggregate centers makes with the z-axis.

Evaluation of the flux [Eq. (21)] with appropriate expressions for the forces F_{ρ}, F_z and for the charge q shows that the second term (axial flux) is always negligible under considered approximations $\Phi << 1$, $r_a >> 1$, while the first term (radial flux) reads:

$$J \approx -\frac{n\zeta_{\perp}\mu_0 M^2 V^2}{2a^2} r_a \times \\ \times \int_0^{z_0} \left(2\left(\alpha^2 + (r_a^{\,2} - 1)z^2\right)^{-3/2} - \left(\alpha^2 - z^2 + r_a^{\,2}(z + 2a)^2\right)^{-3/2} - \left(\alpha^2 - z^2 + r_a^{\,2}(z - 2a)^2\right)^{-3/2} \right)(\alpha^2 - z^2)dz \qquad (24)$$

Estimation of this integral is presented in detail in Appendix C, and the final result for the aggregate flux reads:

$$J = \frac{\Phi \mu_0 M^2}{6\eta_0} \frac{\ln r_a}{r_a^{\,2}} \left(\frac{25\sqrt{5}}{24\Phi^{2/3} r_a^{\,2}} + 1 \right)^{-1}. \qquad (25)$$

The aggregate aspect ratio r_a and its logarithm are related to the aggregate volume by Eqs. (13), therefore the time interval of the i-th coalescence step is related to the volume V_i, as follows:

$$\tau_i \approx J_i^{-1} \approx \tau^* \left(\frac{7\varepsilon}{\ln(V_i / B)} + \frac{7^{1/7} (V_i / B)^{2/7}}{\ln^{1/7}(V_i / B)} \right) \qquad (26)$$

where $\varepsilon = 25\sqrt{5}/(24\Phi^{2/3})$ and $\tau^* = 6\eta_0/(\Phi \mu_0 M^2)$ is a characteristic timescale of the coalescence stage with the aggregate magnetization, M, independent of r_a and V_i thanks to negligible demagnetizing effects in the high aspect ratio limit, $r_a >> 1$. The total elapsed time corresponding to k successive coalescence steps is obtained by summing up the durations τ_i and using $V_i = 2^i V_\tau$:

$$t_k = \sum_{i=0}^{k-1} \tau_i = \tau^* \sum_{i=0}^{k-1} \left(\frac{7\varepsilon}{\ln(2^i \hat{V}_\tau)} + \frac{7^{1/7} (2^i \hat{V}_\tau)^{2/7}}{\ln^{1/7}(2^i \hat{V}_\tau)} \right), \qquad (27)$$

where $\hat{V}_\tau = V_\tau / B$ and $B \sim \pi^3 v / 64$ as it was defined below Eq. (12), v is the volume of individual nanoparticle. The sum in Eq. (27) admits the following approximate expression with a maximal deviation of 3.7% from the exact numerical result:

$$t_k \approx \tau^* \left(\frac{7\varepsilon}{\ln 2} \ln \left(\frac{\ln(2^k \hat{V}_\tau)}{\ln \hat{V}_\tau} \right) + \frac{7^{1/7} \hat{V}_\tau^{\,2/7}}{\ln^{1/7}(2^{k-1} \hat{V}_\tau)} \frac{2^{2k/7} - 1}{2^{2/7} - 1} \right). \qquad (28)$$

Finally, using $2^k = V_k / V_\tau$ in the last equation, and moving form a discrete variation of the volume to a continuous variation, valid at $k >> 1$ (omitting subscripts k at V_k and t_k), we get the following expression for the elapsed time t as function of the dimensionless volume $\hat{V} = V / B$:

$$t \approx \tau^* \left(\frac{7\varepsilon}{\ln 2} \ln \left(\frac{\ln \hat{V}}{\ln \hat{V}_\tau} \right) + \frac{7^{1/7}}{2^{2/7} - 1} \cdot \frac{\hat{V}^{2/7} - \hat{V}_\tau^{\,2/7}}{\ln^{1/7} \hat{V}} \right) \qquad (29)$$

Theoretical dependency of the dimensionless aggregate volume $\hat{V}$ on the dimensionless elapsed time $\hat{t} = t / \tau^*$ is plotted in double logarithmic scale in Fig. 4 for the values $\varepsilon = 10^4$ and $\hat{V}_\tau = 10^7$ typical for our experiments.

The solid curve in that figure corresponds to the general expression Eq. (29) derived for any value of the parameter $r_a^{\,3}\Phi$ but in the limits $\Phi << 1$ and $r_a >> 1$. The shape of this curve is explained by the behavior of two terms of Eq. (29). The first term in the brackets of Eq. (29) is dominant in the beginning of the coalescence process when the aggregates are still small enough and the strong inequality $r_a^{\,3}\Phi << 1$ holds. This term corresponds to the point dipole approximation and gives an initial very slow linear increase of the aggregate volume

$V \approx V_\tau(1+\ln 2/(7\varepsilon)\times(t/\tau^*))$ at $t/\tau^* << 7\varepsilon/\ln 2 << 10^5$, followed by an extremely fast growth with time $V \approx V_\tau^{\exp(\ln 2/(7\varepsilon)\times t/\tau^*)}$ at $t/\tau^* \approx 7\varepsilon/\ln 2 \approx 10^5$. However, at longer times, the aggregates become very long and the second term of Eq. (29) becomes dominant when the distance between aggregates is much shorter than their length, implying the strong inequality $r_a^3\Phi >> 1$. This second term gives a power-law growth of the aggregate volume with time, $V \sim V_\tau(t/\tau^*)^{7/2}$ at $t/\tau^* >> 7\varepsilon/\ln 2 >> 10^5$, explaining a final linear part of the $\hat{V}(\hat{t})$ dependency with a slope 7/2 in double logarithmic scale. Both asymptotic behaviors at $r_a^3\Phi << 1$ and $r_a^3\Phi >> 1$ corresponding to two terms of Eq. (29) are shown in Fig. 4 by dotted and dashed lines, respectively.

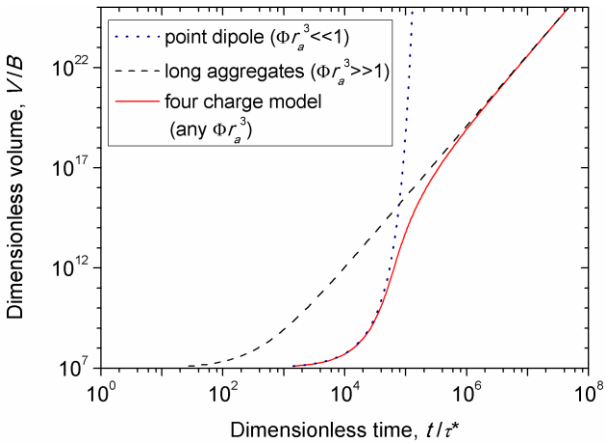

Fig. 4. Theoretical dependences of the dimensionless aggregate volume on the dimensionless time for the aggregate coalescence stage. The following parameters were used in calculations: $\hat{V}_\tau = 10^7$, $\varepsilon = 10^4$.

C. Transition between growth and coalescence stages

The transition from the aggregate growth stage (at shorter times) to the coalescence stage (at longer times) could be found by a simple approach based on comparison of aggregation rates, *dV*/*dt*, of both stages. The transition is supposed to take place at some volume V_τ corresponding to the equality of the aggregation rates of two stages; the aggregate growth takes place at $V<V_\tau$ and coalescence – at $V>V_\tau$. The aggregation rate for the growth stage is directly given by Eq. (14), while the rate for the coalescence stage is obtained by derivation of Eq. (29) with respect to $\hat{V}$: $d\hat{V}/dt = \left(dt/d\hat{V}\right)^{-1}$. The equality of aggregation rates gives the following transcendent equation for the dimensionless transition volume $\hat{V}_\tau$:

$$\frac{4\pi\kappa}{K\varphi''}\left(\frac{D}{B^{2/3}}\right)\frac{\hat{V}_\tau^{3/7}}{(\ln\hat{V}_\tau)^{5/7}}\left(\Delta_0 - \varphi''\Phi_0\frac{\hat{V}_\tau}{\hat{V}_0}\right) = \frac{1}{\tau^*}\left[\frac{7\varepsilon}{\ln 2}\cdot\frac{1}{\hat{V}_\tau\ln\hat{V}_\tau} + \frac{2\times 7^{-6/7}}{2^{2/7}-1}\cdot\frac{1}{\hat{V}_\tau^{5/7}\ln^{1/7}\hat{V}_\tau}\right]^{-1}, \quad (30)$$

recalling that the correction factor *K* is given as function of the magnetic field parameter ξ by Eq. (B-6b) in Appendix B and $\tau^* = 6\eta_0/(\Phi_\tau\mu_0 M^2) = 6\eta_0/(\Phi_0\hat{V}_\tau\mu_0 M^2)$.

Once the value of $\hat{V}_\tau$ is obtained from numerical solution of Eq. (30), the elapsed time covering both phase separation stages is obtained from Eqs. (19) and (29) taking into account

that the initial time of the coalescence stage corresponds to the final time of the growth stage at $\hat{V} = \hat{V}_\tau$:

$$t \approx \begin{cases} \dfrac{K}{4\pi\kappa}\left(\dfrac{B^{2/3}}{D}\right)\dfrac{\hat{V}_0}{\Phi_0}\dfrac{(\ln\hat{V})^{5/7}}{\hat{V}^{3/7}} f\left(\dfrac{\Delta}{\Delta_I}\right)\ln\dfrac{\Delta_I}{\Delta}, & \hat{V} \le \hat{V}_\tau; \\ \dfrac{K}{4\pi\kappa}\left(\dfrac{B^{2/3}}{D}\right)\dfrac{\hat{V}_0}{\Phi_0}\dfrac{(\ln\hat{V}_\tau)^{5/7}}{\hat{V}_\tau^{3/7}} f\left(\dfrac{\Delta_\tau}{\Delta_I}\right)\ln\dfrac{\Delta_I}{\Delta_\tau} + \tau^*\left(\dfrac{7\varepsilon}{\ln 2}\ln\left(\dfrac{\ln\hat{V}}{\ln\hat{V}_\tau}\right) + \dfrac{7^{1/7}}{2^{2/7}-1}\cdot\dfrac{\hat{V}^{2/7}-\hat{V}_\tau^{2/7}}{\ln^{1/7}\hat{V}}\right), & \hat{V} > \hat{V}_\tau, \end{cases} \quad (31)$$

where $\Delta_I = \Delta_0 - \varphi''\Phi_0$, $\Delta_\tau = \Delta_0 - \varphi''\Phi_0\hat{V}_\tau/\hat{V}_0$, $\Delta = \Delta_0 - \varphi''\Phi_0\hat{V}/\hat{V}_0$ [Eq. (17)], and the correction factor $f(\Delta/\Delta_I)$ is given by Eq. (19-b).

The behavior of Eq. (31) is inspected in details in Sec. IV, in which it is tested against experimental results, and the validity and drawbacks of the current approach (based on comparison of aggregation rates) are discussed.

III. Experiments

In experiments, the phase separation process was visualized using an optical microscopy. The main goal was to determine the aggregate size as function of the elapsed time, the magnetic field intensity and the initial particle volume fraction.

A suspension (ferrofluid) of iron-oxide nanoparticles dispersed in distilled water and covered by a double layer of oleate salts has been synthesized using a conventional method of co-precipitation of iron salts in alkali medium[21,72]. This synthesis gave permanent nanoclusters of nearly spherical shape and composed of numerous nanoparticles likely because of a rapid and uncontrolled kinetics of adsorption the second oleate layer[55]. The nanoclusters have a relatively broad size distribution ranging from 20 to 220 nm with the average size equal to 54 nm, as inferred from dynamic light scattering [Fig. S1 in Supplementary Material]. This size corresponds to the gravitational Péclet number $Pe_G \approx 3\times10^{-5}$, defined as the ratio of the diffusion time to the sedimentation time, and confirming a good stability of the suspension against gravitational sedimentation. The saturation magnetization of the solid phase of nanoclusters was measured by vibrating sample magnetometry and found to be M_S=481 kA/m, the value closed to that of the bulk magnetite. The details of the nanoclusters' synthesis and characterization are given in Supplementary Material. To avoid any confusion between nanoclusters and aggregates, the former are hereinafter called magnetic particles or shortly particles.

The minimum particle volume fraction φ' at which the suspension undergoes phase separation at a given magnetic field was measured by direct visualization of the suspension structure. To this purpose, the synthesized ferrofluid was diluted by distilled water at different particle volume fractions φ ranging from 8×10^{-6} to 3×10^{-3} (8×10^{-4} – 0.3%vol.). Each suspension was injected to a transparent cell of a size 20×10×0.2 mm sketched in Fig. 5 and formed by a Plexiglas substrate and a microscope glass slide separated from each other by a polyvinyl seal. The cell was placed into a transmitted light inverted microscope Nikon Diaphot-TMD (Japan) equipped with a complementary metal oxide semiconductor (CMOS) camera PixeLINK PL-

B742U (Canada). An external homogeneous magnetic field was generated by a pair of Helmholtz coils placed around the microscope and was applied parallel to the thin layer of the suspension inside the cell. The observation of the suspension structure was carried out using a 50-fold objective (Olympus LMPlanFl 50×0.50) with a large working distance, allowing detection of aggregates of a minimum size about 1 μm.

In the absence of external magnetic field, the suspensions were homogeneous on the length scale 1μm of the microscope optical resolution. When a strong enough magnetic field was applied, long and thin particle aggregates of a size above 1 μm and aligned with the direction of the applied magnetic field rapidly appeared and grew with time, as shown in Fig. 7 of Sec. IV-B. If the applied magnetic field was not strong enough, the aggregates were not observed for at least half an hour. The threshold field H at a given concentration φ was determined as a medium value of two closest magnetic fields H_1 and H_2 at which the aggregates were not and were observed during 30 min, while the uncertainty was estimated as $(H_2 - H_1)/2$. The obtained experimental dependency $\varphi'(H)$ will be analyzed in Fig. 6 of Sec. IV-A.

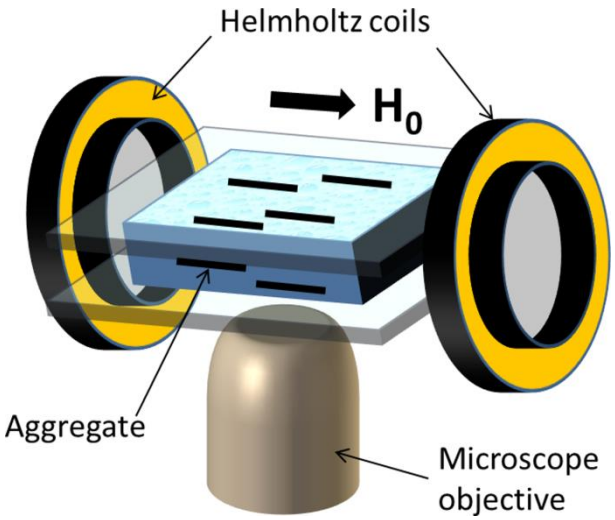

Fig. 5. Sketch of the experimental setup. The ferrofluid sample is squeezed between a lower Plexiglas and an upper glass plates separated from each other by a polyvinyl seal (not shown here).

A similar experimental setup [Fig. 5] was used for measurements of the aggregate size during phase separation. Upon application of the external magnetic field of a desired intensity H_0, the aggregation process was recorded for 20 min and snapshots were taken each one minute. The measurements were performed for the suspensions of initial particle volume fraction φ_0=1×10^{-3}, 2×10^{-3} and 3×10^{-3}, and for the magnetic field intensities H_0=0.78, 2.75 and 4.0 kA/m. The observed microstructure will be analyzed in Sec. IV-B. To draw quantitative conclusions, the snapshots were processed by the ImageJ software. The aggregate size and shape were characterized by the following magnitudes: (a) a tip-to-tip length 2a called the aggregate length [Fig. 1]; (b) a width 2b at the half-length [Fig. 1]; (c) the aggregate volume, supposing its ellipsoidal shape, $V = 4\pi ab^2/3$; and (d) the aggregate aspect ratio $r_a = (2a)/(2b)$. Because of a limited number of aggregates per observation window, it was rather challenging to obtain a smooth distribution function of their size, and we restricted our analysis to arithmetic averages $\langle 2a \rangle$, $\langle 2b \rangle$, $\langle V \rangle$ and $\langle r_a \rangle$ of the measured quantities defined in different focal planes of the

sample. The evolution of these quantities with time will be analyzed in Sec. IV-C for different values of H_0 and φ_0. Uncertainties on these quantities were estimated as a sum of the standard deviation between three independent measurements and the error related to focusing and sharpness of the aggregate border.

IV. Results and discussion

A. Binodal curve

The experimental dependency $\varphi'(H)$ obtained at relatively long elapsed times (when the particle aggregation seemed to stop) is shown in double logarithmic scale in Fig. 6. The region below this curve corresponds to the dilute gas-like suspension phase of the suspension. The region above and on the right from this curve corresponds to a mixture between the dilute and the concentrated liquid-like or solid-like phases. The technique described in Sec. III does not allow determination with confidence of the second coexistence curve $\varphi''(H)$. The shape of the $\varphi'(H)$ curve has some similarities with the shape of the corresponding coexistence curve of the phase diagram calculated by Hynninen and Dijkstra[42] for dipolar hard spheres. A step in the middle of the binodal curve could stand for transition between entropically driven[73] to magnetically driven phase transition, as inferred from our previous study[57]. In our case, this curve was fitted by the following empirical formula, valid in the concentration range $8\times10^{-6} < \varphi' < 3\times10^{-3}$ and in the range of the magnetic field intensities $150 < H < 12500$ A/m:

$$\varphi'(H) = \begin{cases} \dfrac{a_1 H}{H - h_1}, & 150 < H < 3030 \text{ A/m}; \\ \varphi_1 + \dfrac{\varphi_2 - \varphi_1}{1 + e^{a_2 (H - h_2)}}, & 3030 < H < 12500 \text{ A/m}, \end{cases} \tag{32}$$

where the magnetic field intensity H is in A/m and the fitting parameters take the following values: $a_1 = 5.05\times10^{-4}$, $a_2 = 2.90\times10^{-3}$ A^{-1}m, $h_1 = 133$ A/m, $h_2 = 3330$ A/m, $\varphi_1 = 8.259\times10^{-6}$, $\varphi_2 = 7.072\times10^{-4}$. The fitting curve [Eq. (32)] is shown in Fig. 6 by a continuous line.

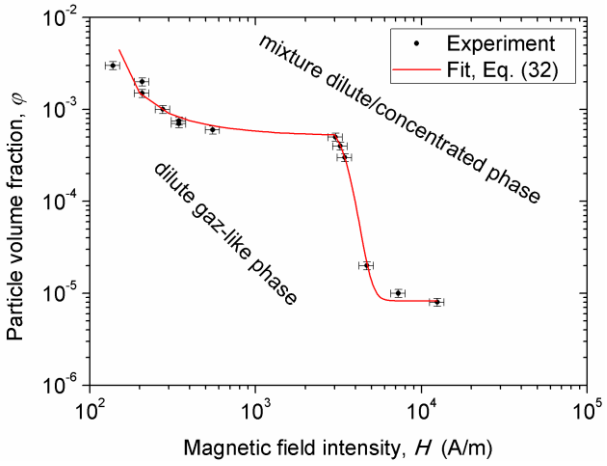

Fig. 6. Experimental φ-H phase diagram of the nanoparticle suspension in the presence of a uniform magnetic field. Only one of the coexistence curves, $\varphi'(H)$, is available in experiments. Another coexistence curve $\varphi''(H)$ is unavailable and not shown here. The error bars correspond to the sum of the standard deviation on three independent measurements and of uncertainties of measurements of H and φ.

It is important to notice that the measured values of the threshold magnetic field correspond to unexpectedly low values of the magnetic field parameter ξ [Eq. (10)] and of the dipolar coupling parameter $\lambda = \beta_p \xi / 4$ (both ranged between 10^{-2} and 10). The phase separation in magnetic colloids is usually expected at λ>1 and ξ>1 and the reason for the phase separation at λ<1 and ξ<1 very likely comes from relatively high polydispersity of magnetic particles, as discussed in details in Sec. IV-E.

B. Microstructure

Snapshots of the suspension microstructure at different elapsed times are shown in Fig. 7 for the intensity of the applied magnetic field H_0=4.0 kA/m. The three columns correspond to the three studied initial particle volume fractions φ_0=1×10^{-3}, 2×10^{-3} and 3×10^{-3}. The first raw corresponds to the initial moment of time t=0 at which the magnetic field was applied to initially homogeneous suspension in the direction horizontal with respect to the page.

Upon the field application, elongated drop-like aggregates aligned with the applied magnetic field appear and are already distinguishable at the elapsed time t=1min (second row in Fig. 7). This means that the initial nucleation stage is very short and unobservable in our optical microscopy experiments. The aggregate size increases progressively with time. At relatively short times, t<5 min, the growth of individual aggregates is observed, certainly thanks to adsorption of magnetic particles from the surrounding fluid. At longer times, t>5 min, neighboring aggregates start to coalesce because of their dipolar interactions, when their length is comparable to the average distance between them. Coalescence seems to accelerate the aggregate growth until t≈15 min. However, at t>15 min, the average aggregate length becomes much longer than the distance between them and the coalescence rate seems to decrease, at least at the considered field, H_0=4 kA/m, likely because of repulsive dipolar interactions between aggregates.

Because of insufficient optical resolution, it was impossible to retrieve exact aggregate shape. Qualitatively, the aggregate width progressively decreases when moving from the aggregate center to the tips, as in the case of ellipsoidal shape supposed in the model. Conical spikes have not been detected on aggregate tips, as opposed to the experiments of Promislow and Gast[30] on drop-like aggregates of magnetorheological fluids and to our previous experiments on phase condensation around a magnetized micro-bead[55,57]. In fact, the characteristic period $\Pi = \left(D\eta_0 / (\Delta\rho_a g) \right)^{1/3}$ of patterns arising during convective instability on the interface between two miscible magnetic phases[74] is about one micron for our experimental case (here $\Delta\rho_a$ is the difference between the aggregate and the surrounding medium densities). This length scale is comparable to the aggregate width, such that the aggregate tip is likely unable to develop numerous spikes.

As expected, at increasing initial particle volume fraction φ_0, the aggregate size increases at a given elapsed time. The effect of the volume fraction and of the applied magnetic field on the aggregation state of the suspension can be better inspected on Fig. 8 where, all the snapshots are presented for the same elapsed time, equal to t=20 min but for three different values of φ_0 and H_0. The suspension structure does not seem to change qualitatively with variations in φ_0 and H_0: more or less long aggregates, extended along the applied magnetic field are observed for all

studied concentrations and fields. However, the aggregate length and thickness seem to increase considerably with increasing magnetic field and initial particle concentration and this effect will be inspected in detail in Sec. III-C.

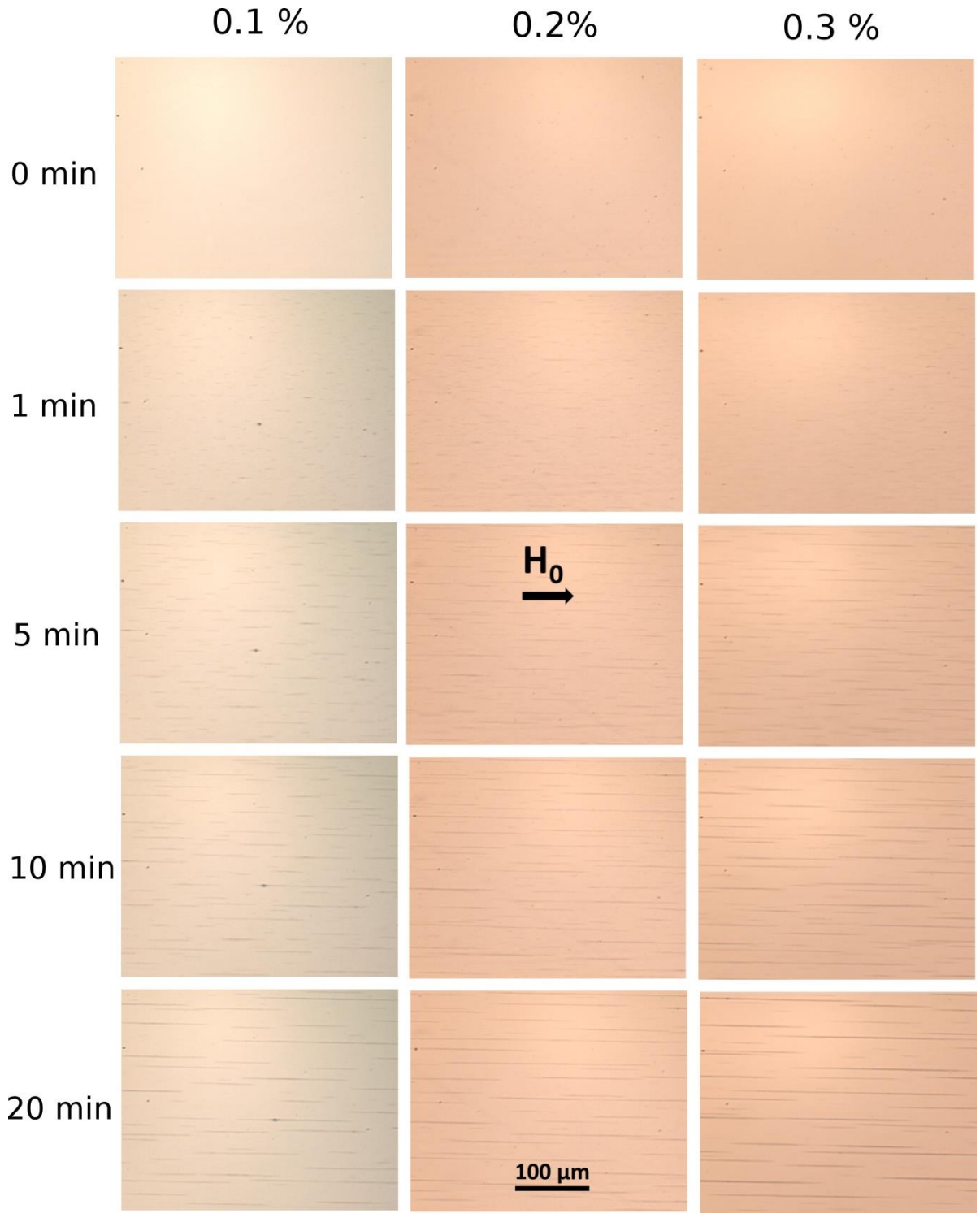

Fig.7. Snapshots of the suspension microstructure at different elapsed times (different rows), for three initial particle concentrations φ_0 (different columns) and for the intensity of the applied magnetic field H_0=4.0 kA/m

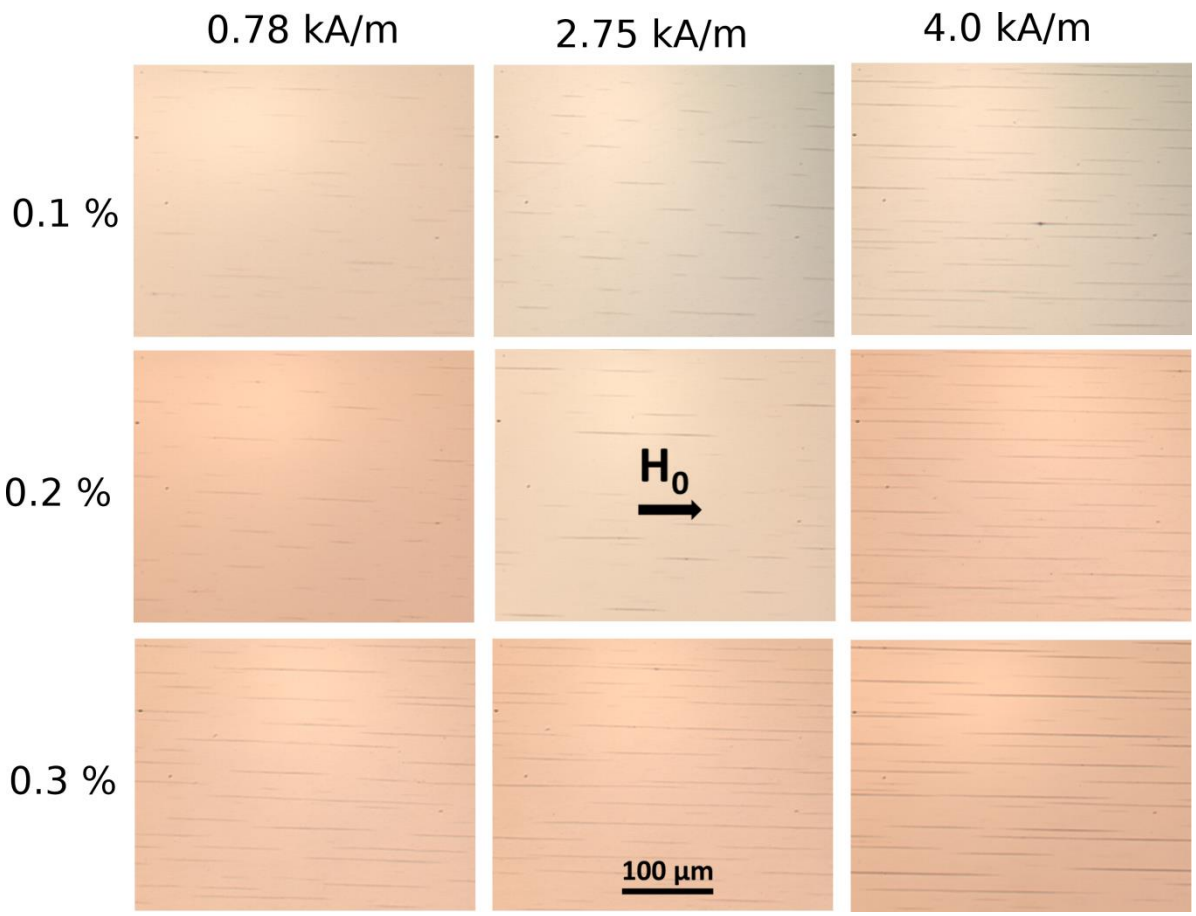

Fig. 8. Snapshots of the suspension microstructure at the fixed elapsed time equal to t=20 min and different intensity H_0 of the applied magnetic field and different initial particle concentrations φ_0.

It is important to notice that the aggregates have a thickness of a few microns and the length of several hundreds of microns. Note that the aggregate thickness is governed by the interplay between magnetic and surface energy of the aggregates leading to Eq. (12) relating the aggregate volume to its shape. Their gravitational Péclet number is of the order of $Pe_G \sim 10^2$ and their sedimentation time (required for a horizontal aggregate to fall a distance equal to its width) is equal to a few seconds, so the aggregates are expected to sediment and reach the bottom of the cell during a few minutes. However, the images at different horizontal planes show that there are no aggregates near the bottom and the upper walls of the cell within boundary layers of a characteristic thickness of about 10 µm. This could be tentatively explained by magnetic levitation of aggregates dispersed in a dilute ferrofluid, when the lines of the magnetic field induced by the aggregate are "repelled" from non-magnetic walls and create an effective repulsion of the aggregate from the cell walls, by analogy with levitation of magnets in ferrofluids[21].

C. Aggregate size

Our model was mostly focused on calculations of the elapsed time as function of the aggregate volume V. The three remaining geometrical parameters of the aggregates are easily related to the aggregate volume using Eqs. (11), (13). Thus, the aggregate aspect ratio r_a is directly given by Eq. (13b), while the aggregate length and width are given by the following expressions:

$$2a = 2\left(\frac{3}{4\pi} V r_a^{\,2}\right)^{1/3} = 2\left(\frac{3}{4\pi}\right)^{1/3} \hat{V}^{3/7} \left(\frac{1}{7}\ln\hat{V}\right)^{2/7} B^{1/3}, \qquad \text{(33-a)}$$

$$2b = 2\left(\frac{3V}{4\pi r_a}\right)^{1/3} = 2\left(\frac{3}{4\pi}\right)^{1/3} \hat{V}^{2/7} \left(\frac{1}{7}\ln\hat{V}\right)^{-1/7} B^{1/3}. \qquad \text{(33-b)}$$

The most precise measured quantity describing the aggregate size is the average aggregate length $\langle 2a \rangle$. Theoretical and experimental dependencies of the average aggregate length on elapsed time are presented in Figs. 9 a-c for three different values of the intensity H_0 of the applied magnetic field and for the three different initial particle volume fractions φ_0 of the suspension. The most of experimental curves show an initial sublinear increase of the aggregate length with time, followed by a change in the slope at t≈10-15 min and by a stronger increase. Qualitatively, such a change of the slope corresponds to a transition between the aggregate growth and the aggregate coalescence regimes, as checked by tracking the snapshots [Fig. 7]. Since in experiments the aggregates had unequal lengths, the transition was progressive, i.e. occurred within finite lapses of times and aggregate volumes. Experiments also show that at the same elapsed times, the aggregate length is an increasing function of the magnetic field intensity H_0 and of the initial particle volume fraction φ_0. This means that the aggregation process accelerates with increasing H_0 and φ_0. This was expected because an increasing magnetic field enhances dipolar particle-particle, particle-aggregate and aggregate-aggregate interactions, while an increasing particle concentration reduces the time of approach of two particles and of two aggregates.

The theoretical dependence of the average aggregate length $\langle 2a \rangle$ on time is found in parametric form $\{\langle 2a \rangle = f_1(V), t = f_2(V)\}$ [Eqs. (33-a), (31)] and is presented by solid lines in Fig. 9. The aggregate magnetization M intervening into the timescale τ^* of the coalescence stage was calculated in a linear approximation, $M \approx \chi H_0$ with the aggregate magnetic susceptibility estimated using the Maxwell-Garnett mean field theory[71]: $\chi = 3\beta_p\varphi''/(1-\beta_p\varphi'') \approx 3\varphi''/(1-\varphi'') \approx 4.5$, where $\beta_p \approx 1$ [cf. definition below Eq. (4)] and $\varphi'' \approx 0.6$ - the internal volume fraction of aggregates [cf. Sec. II-A]. Two remaining unknown parameters, $\hat{V}_0$ and Φ_0 were found by fitting the experimental $\langle 2a \rangle$ versus t dependences by theoretical ones. Both these parameters have been found to strongly vary with the magnetic field intensity H_0 and the initial particle volume fraction φ_0. The initial aggregate concentration Φ_0 is expected to be proportional to the concentration of the condensation centers in the suspension and is assumed to vary linearly with φ_0: $\Phi_0 = \Theta\varphi_0$. On the other hand, depending on the kinetics of the early nucleation stage, the initial dimensionless volume $\hat{V}_0$ of aggregates could be an increasing function of both the magnetic field parameter ξ and the initial particle volume fraction φ_0. We have supposed the empirical correlation $\hat{V}_0 = \vartheta\xi\varphi_0^{\,2}$ for $\hat{V}_0$, which allows a reasonable agreement with experiments. Thus, all the nine experimental curves shown in Fig. 9 have been

fitted to the theory using the aforementioned expressions for Φ_0, $\hat{V}_0$ and the single set of adjustable parameters Θ and ϑ. The best fit was obtained at $\Theta = 3.3\times10^{-4}$ and $\vartheta = 5.0\times10^{12}$.

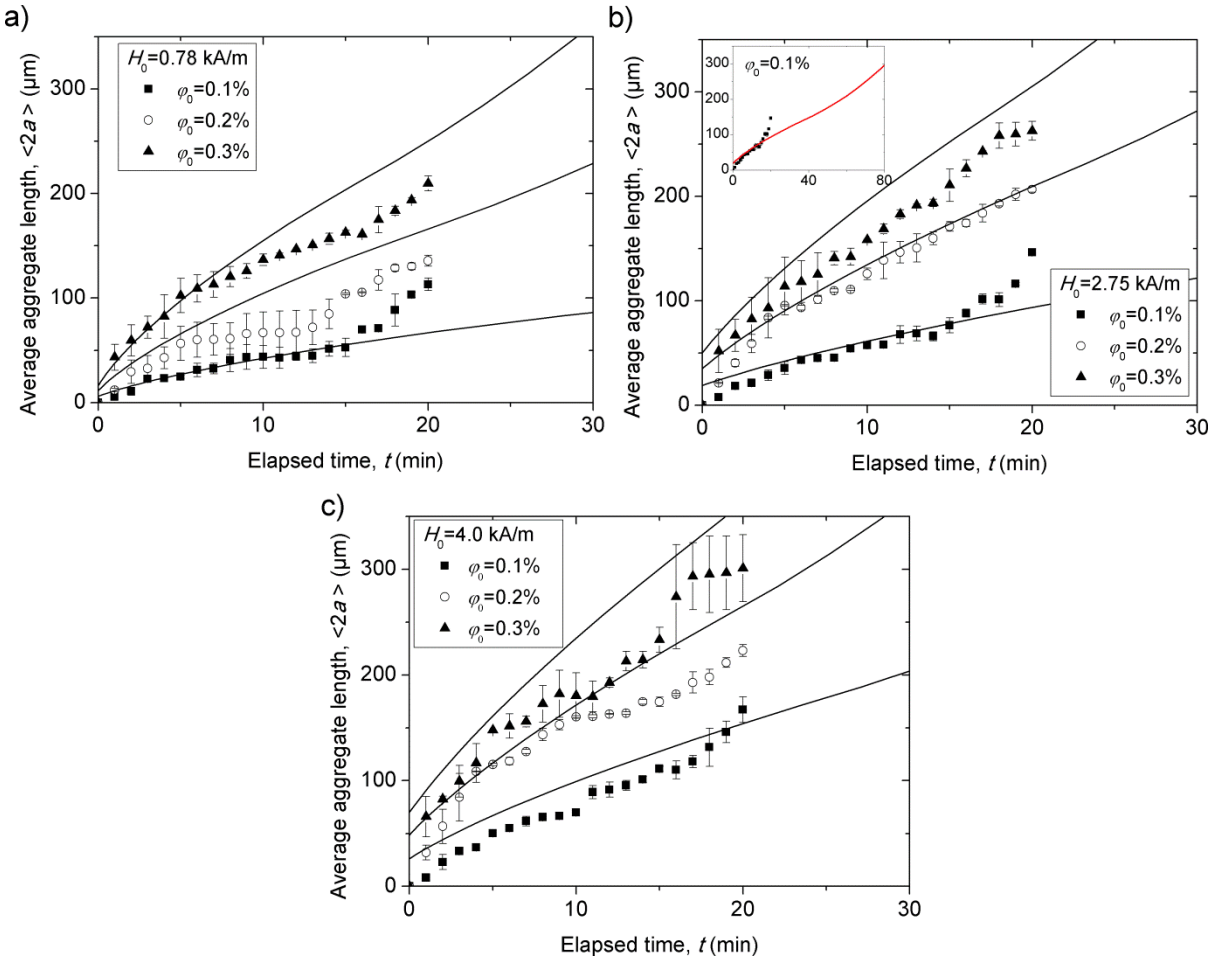

Fig. 9. Experimental and theoretical dependences of the average aggregate length on the elapsed time for different initial particle concentrations φ_0 and different magnetic field intensities H_0=0.78 kA/m (a); 2.75 kA/m (b); 4.0 kA/m (c). Symbols stand for the experiments, solid lines – for the theory. The inset in (b) shows the same dependency for φ_0=0.1% in extended time scale. The experimental results were fitted by the theoretical dependences with the values of the adjustable parameters: $\Theta = 3.3\times10^{-4}$ and $\vartheta = 5.0\times10^{12}$.

Our model seems to qualitatively reproduce the main experimental behaviors. First, one can distinguish a change of the behavior of the $\langle 2a \rangle$ versus t theoretical curves from sublinear to stronger than linear dependency. This change corresponds to the transition between two aggregation stages. The slope changes in a less abrupt manner than in experiments but rather continuously according to the proposed scenario of the transition based on equality of the aggregation rates [Sec. II-C]. The change of the slope can be better appreciated in inset of Fig.9b, where $\langle 2a \rangle$ versus t dependence is plotted for broader range of the elapsed times at H_0=2.75 kA/m and φ_0=0.001. Second, the model captures the increasing dependence of the aggregate length on the applied field H_0. The magnetic field accelerates both stages of the phase separation. During the aggregate growth stage, it decreases the correction factor K responsible for magnetophoretic particle flux and increases initial supersaturation $\Delta_0 = \varphi_0 - \varphi'$ through a decrease of the equilibrium dilute phase concentration $\varphi'(H_0)$ according to Eq. (32) and Fig. 6.

Since the aggregate growth rate *dV*/*dt* is proportional to the ratio $\Delta / K = (\Delta_0 - \varphi"\Phi)/K$ [Eq. (14)], both effects contribute to the increase of the aggregation rate with an increasing magnetic field. The effect of Δ_0 is found to dominate over the effect of *K* within our experimental ranges of H_0 and φ_0 because *K* is a weakly (logarithmically) decreasing function of ξ and therefore of H_0 [Eq. (B-6b) in Appendix B]. During the coalescence stage, the magnetic field decreases significantly the timescale of the process proportionally to the square of the aggregate magnetization *M*, thus to the square of the applied field: $\tau^* \propto M^{-2} \propto H_0^{-2}$. Third, the model predicts an increase of the aggregate length with the initial particle volume fraction φ_0. During the aggregate growth stage, the aggregation rate is proportional to the supersaturation $\Delta = \Delta_0 - \varphi"\Phi \propto \varphi_0$ [Eq. (14)], thus, it increases linearly with φ_0. During coalescence stage, both terms of the elapsed time are proportional to $\Phi^{-5/3}$ and Φ^{-1} respectively [Eq. (29)], implying an increasing growth rate with increasing φ_0. In addition to it, higher initial aggregate volumes $\hat{V}_0 \propto \xi \varphi_0^{\,2} \propto H_0^{\,2} \varphi_0^{\,2}$ at higher applied fields and higher initial concentrations also lead to an increase of the aggregate length with the growth in H_0 and φ_0.

Quantitative discrepancy between the theory and experiments could come from different assumptions of the model. For example, a slower variation of the aggregate size than that observed in experiments at *t*>15 min likely arises because of underestimation of the coalescence rate using the cell model [cf. Sec. II-B]. On the other hand, step-like shape of some experimental curves could be a result of insufficient number of aggregates at long elapsed times when individual coalescence events (resulting in a step-wise increase of the aggregate size) are not sufficiently frequent for obtaining a smooth variation of the aggregate size.

The behavior of other geometrical parameters, $\langle 2b \rangle$, $\langle r_a \rangle$ and $\langle V \rangle$, were also inspected and plotted as function of time in Figs. 10a and b for the magnetic field H_0=2.75 kA/m and the initial particle volume fraction φ_0=0.001. For the sake of comparison, the aggregate length $\langle 2a \rangle$ is also plotted in Fig. 10a. We remark that the aggregate width $\langle 2b \rangle$ exhibits a slower growth with time than the aggregate length $\langle 2a \rangle$: in experiments the length increases from 0 to 150 μm, while the width – from 0 to 2.6 μm [symbols on Fig. 10a]. This trend is confirmed by our model [lines in Fig. 10a] and is explained by minimum energy principle (valid for individual aggregates under local equilibrium assumption) leading to the scaling laws $\langle 2a \rangle \propto V^{3/7}$ [Eq. (33-a)], $\langle 2b \rangle \propto V^{2/7}$ [Eq. (33-b)] and showing that the length increases stronger than the width with the aggregate volume, and therefore with time. Even though experimental determination of the aggregate width is subjected to relatively large errors, our model systematically overestimates it. This is likely because of overestimation of the aggregate surface tension Σ, and thus of the volume scale $B \propto \Sigma^3/(\mu_0 M^2)^3 \approx \pi^3 v/64$ [Eq. (12)]. Such overestimation is expected to promote thicker aggregates with a smaller aspect ratio, as compared to those observed in experiments – see Fig. 10b for $\langle r_a \rangle$. The model reproduces qualitatively the shape of the experimental $\langle V \rangle$ versus *t* dependency, but since it overestimates the aggregate thickness by a factor of about 1.7, it

overestimates the aggregate volume $\langle V \rangle \propto \langle b^2 \rangle$ by a factor of 3. A better agreement between theory and experiments should be obtained in future in frames of a more precise model based on determination of the aggregate size distribution.

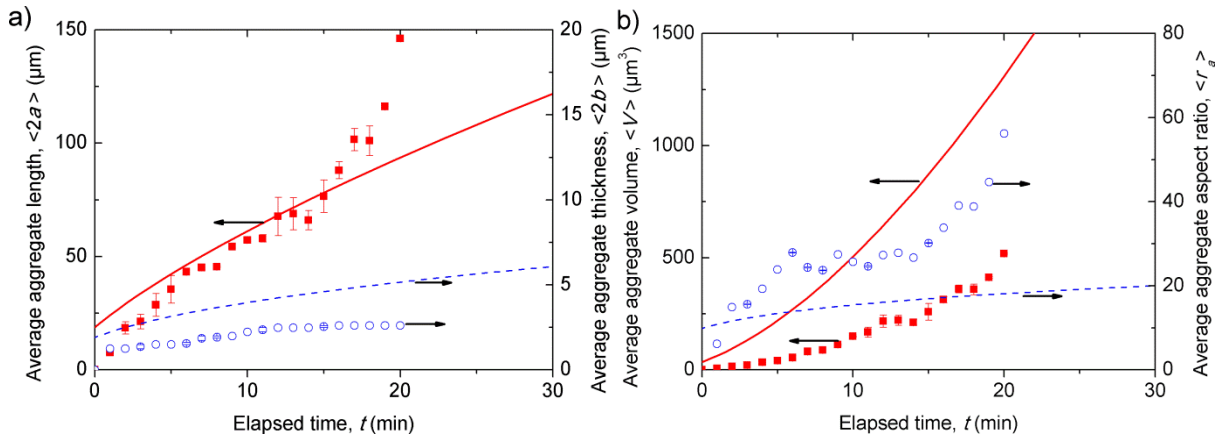

Fig. 10. Experimental and theoretical dependences of the average aggregate length and width (a), as well as of the average aggregate volume and aspect ratio (b) on the elapsed time for the magnetic field intensity H_0=2.75 kA/m and the initial particle volume fraction φ_0=0.1%. Symbols stand for the experiments, solid lines – for the theory. The experimental results were fitted by the theoretical dependences with the same values of the adjustable parameters, as the one used for fitting the data on Fig. 9.

D. Aggregate concentration

Another important parameter that can be retrieved from our model is the aggregate concentration Φ, which changes with time, at least during the aggregate growth stage when the aggregates absorb individual particles from the surrounding fluid. In our model, the aggregate concentration is related to the dimensionless aggregate volume by the following equation:

$$\Phi = \begin{cases} \Phi_0 \hat{V} / \hat{V}_0, & \hat{V} \le \hat{V}_\tau \\ \Phi_0 \hat{V}_\tau / \hat{V}_0 = const, & \hat{V} > \hat{V}_\tau \end{cases} \qquad (34)$$

where the upper expression corresponds to the aggregate growth stage, the lower expression – to the coalescence stage and the volume $\hat{V}$ at the transition is found by numerical solution of Eq.(30).

Theoretical dependence of the aggregate concentration on the elapsed time is obtained in parametric form $\left\{\Phi = f_1(\hat{V}), t = f_2(\hat{V})\right\}$ [Eqs. (34), (31)] and is plotted in Fig. 11 for the magnetic field intensity H_0=4 kA/m and for three different initial particle volume fractions φ_0. In the beginning, the aggregate concentration increases stronger than linearly with time during the aggregate growth stage proportionally to the aggregate volume. Then, above the transition point, it becomes independent of time and the curves show a final horizontal plateau. As expected, at the same elapsed time, the aggregate concentration increases with the initial particle volume fraction φ_0 because the initial aggregate concentration Φ_0 has been supposed to be proportional to φ_0 in frames of the heterogeneous nucleation scenario.

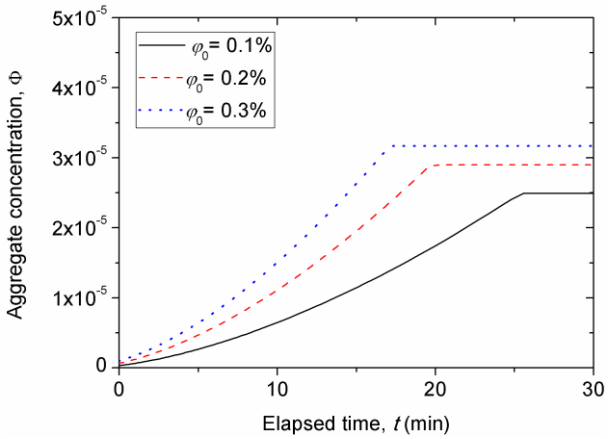

Fig. 11. Theoretical dependence of the aggregate concentration as function of elapsed time for the magnetic field intensity H_0=4.0 kA/m and three different initial particle volume fractions φ_0. For calculations, we have used the same values of the adjustable parameters, as the one used for fitting the data on Fig. 9.

It is important to note that the concentration Φ_τ at the plateau of Φ versus t dependences does not reach the maximal concentration $\Phi_m \approx \Delta_0 / \varphi''$ expected at the equilibrium between the dilute and concentrated phases at the end of the phase separation. For instance, the plateau value for H_0=4 kA/m and φ_0=0.003 is $\Phi_\tau \approx 4.3\times10^{-5}$, while the maximum value is $\Phi_m \approx 9.7\times10^{-3}$, so, it is two orders of magnitude larger than Φ_τ. This means that the particle concentration φ_∞ in the dilute phase does not reach the equilibrium concentration φ' but remains relatively close to the initial particle volume fraction φ_0, implying that the suspension super-saturation Δ does not tend to zero at infinite times, as expected at equilibrium, but decreases insignificantly with respect to its initial value Δ_0.

Such inconsistency could come from the transition scenario developed in Sec. II-C. Apparently, the transition between two stages occurs at relatively low aggregate volumes, $V << V_m$, well below the plateau of the aggregate growth stage [cf. Fig. 2], when the aggregate concentration is still far from the maximum value Φ_m. After transition, during the coalescence stage, possible aggregate growth due to absorption of individual particles is ignored, implying constant aggregate concentration, which is well below the equilibrium value Φ_m. In reality, the aggregates are expected to grow both due to absorption of particles and coalescence.

It is worth noticing that in experiments, the aggregate concentration Φ at long elapsed times also seems to be much lower that the equilibrium value Φ_m. Direct estimation from the micrographs, obtained at different focal plains across the thickness of the observation cell, gives the Φ value of the order of 10^{-4} for t=20 min, H=4 kA/m and φ_0=0.3%, so, two orders of magnitude lower than the equilibrium value $\Phi_m \approx 10^{-2}$. However, the reason of the experimental discrepancy between Φ and Φ_m is rather different from the reasons indicated above for the theoretical discrepancy. The experimental discrepancy is expected to come from particle polydispersity, as discussed in details in the following Sec. IV-E.

E. Possible effects of polydispersity

Polydispersity is expected to have different effects on the phase separation process. First, it leads to the heterogeneous mechanism of the particle nucleation: the biggest particles play the role of the condensation centers for formation of nuclei, as opposed to the homogeneous nucleation occurring in monodisperse suspensions free of any impurity, in which the nuclei are formed by the particles of the same size, as has been described in details in the work of Zubarev and Ivanov[50]. The heterogeneous nucleation is expected to lead to another nucleation rate and other details of the earliest stage, than those for the homogeneous nucleation. The initial stage of heterogeneous nucleation is too short for our system and cannot be detected using the optical microscopy.

Second, the particle polydispersity is expected to result in polydisperse initial nuclei enhancing the degree of polydispersity of final bulk drop-like aggregates. Third, only the largest particles of the polydisperse magnetic colloid are expected to form aggregates. This can be implicitly checked by comparing the fraction of particles $\Phi\varphi''/\varphi_0$ belonging to the aggregates with the fraction of large particles in the suspension. Assuming $\varphi'' \approx 0.6$, we estimate $\Phi\varphi''/\varphi_0 \approx 0.02$ (2%vol). This fraction corresponds to the particles of the size d>150 nm according to the size distribution curve [Fig. S1 in Supplementary Material]. The population of the largest particles has a medium size of about 180 nm and corresponds to the parameters ξ ranged between 1 and 23 for the experimental range of the magnetic fields. These values of ξ are more relevant for the field-induced phase separation described in Sec. IV-A rather than the values of ξ calculated using the average particle size, d=54 nm, of the suspension. The rest of the particles (98 %) do not contribute to the aggregates, such that the dilute phase concentration φ_∞ should not be very different from the initial particle concentration φ_0. This fact is confirmed by the analysis of the transmitted light intensity through the medium between the aggregates. This also explains the difference between the measured value of the aggregate concentration Φ and the maximum value Φ_m that would expected if the particles of all sizes were able to aggregate [cf. Sec. IV-D].

The effect of the polydispersity of the magnetic colloid on the phase equilibrium is often accounted for in a bi-disperse approximation[75,76], with a size ratio and a fraction of largest particles considered as two adjustable parameters of that model. Our assumption that aggregates are mainly constituted by coarse particles is in agreement with the prediction of the bi-disperse model. Bi- or polydispersity of particles would certainly affect the predictions of our kinetic model not only through appearance of unequal aggregates but also through a modification of the time scale $B^{2/3}/D \propto d^3$ and of the initial aggregate concentration Φ_0 and initial supersaturation Δ_0 both depending on the initial concentration of the fraction of largest particles $\varphi_{0L} < \varphi_0$. We believe, however, that our monodisperse approximation gives a satisfactory physical picture of the kinetics of aggregation of medium-sized nanoparticles without introduction of two supplementary adjustable parameters related to the particle polydispersity. The extension to the polydisperse case will be performed in a future work.

V. Concluding remarks

The present paper is focused on theoretical modeling and experimental studies of the kinetics of aggregation of medium sized superparamagnetic nanoparticles (20<d<100 nm) in the presence of an external uniform magnetic field.

In experiments, the kinetics of aggregation was directly observed in the presence of a magnetic field using a transmission light microscope. At initial particle concentrations $\varphi_0 > \varphi'(H_0)$, upon application of an external uniform magnetic field, a suspension of magnetic nanoparticles undergoes a phase separation manifesting by appearance of long needle-like aggregates extended along the direction of the applied field. The aggregate size grows with time, and two distinct aggregation stages are distinguished: (a) growth of individual aggregates by absorption of nanoparticles from the ambient fluid; (b) coalescence of neighboring aggregates occurring at longer elapsed times, while the earliest heterogeneous nucleation stage is too short and cannot be observed in optical microscopy experiments. The beginning of coalescence is accompanied by a change of the slope of the time dependency of the average aggregate length. The aggregation rate appears to increase with increasing magnetic field intensity H_0 and initial particle concentration φ_0.

For the better understanding of each aggregation step, separate theoretical models have been developed for both steps and a transition scenario has then been proposed. First, a kinetic equation including diffusive and magnetophoretic fluxes of the single particles and their adsorption by the aggregate has been developed for the aggregate growth step. The kinetic equation shows a saturation of the aggregate size with time when the dilute phase particle concentration φ_∞ approaches the equilibrium value φ', meaning that the supersaturation $\Delta = \varphi_\infty - \varphi'$ goes to zero. Second, hierarchical model of See and Doi[36] was adapted for coalescence of ellipsoidal aggregates, while possible aggregate growth due to absorption of particles between coalescence steps was neglected. This model predicts stronger than linear increase of the aggregate volume and of the aggregate length with time, with long-time behaviors $\langle V \rangle \propto t^{7/2}$ and $\langle 2a \rangle \propto t^{3/2}$. Both models confirm experimental findings on an increase of the aggregation rate with growing magnetic field intensity and the initial particle volume fraction. However, the magnetic field H_0 has a much stronger effect on kinetics of the coalescence stage (decreasing the timescale τ^* proportionally to H_0^2) than on the kinetics of the aggregate growth stage.

A transition between two aggregation stages was supposed to occur when the aggregation rate of the coalescence regime becomes larger than that of the aggregate growth regime. Such approach gave a reasonable agreement between the theory and experiments for the time dependencies of the aggregate length at different magnetic fields and initial particle concentrations. The agreement was less good for the aggregate width and volume. Another important point is that the model predicts the transition at the aggregate concentrations Φ_τ well below the equilibrium value $\Phi_m \approx \Delta_0 / \varphi''$ and during coalescence stage the concentration is supposed to be constant $\Phi = \Phi_\tau << \Phi_m$. The reason for the experimental discrepancy between Φ

and Φ_m lies in the fact that only the largest particles of the polydisperse colloid contribute to the phase separation.

In summary, the presented model captures the main features of the aggregation process and allows at least semi-quantitative agreement with experimental results. The theory can be further improved by considering particle polydispersity, the early nucleation stage and final Oswald ripening stage, as well as calculating the size distribution of aggregates using either Fokker-Planck or Smoluchowski kinetic equations. New experiments allowing a precise description of the early nucleation stage are necessary to complete the physical picture of kinetics of phase separation in polydisperse suspensions.

Supplementary Material

Materials and Methods. Synthesis and characterization of magnetic nanoparticles are described.

Acknowledgements

The authors acknowledge financial support of French CNRS-INSIS (PEPS program). One of the authors (H. E.) acknowledges FSB through its Ph.D. collaboration fellowship. AZ is grateful to the Program of Ministry of Science and Education of Russian Federation, project 3.1438.2017/PCh.

Appendix A. Spatial distribution of the magnetic field and the particle energy

Both ellipsoidal aggregates and the surrounding fluid are considered as continuous media, with high and low particle concentrations, respectively, and possessing magnetic susceptibilities equal to χ_a and zero, respectively. The magnetostatic potential Ψ around the aggregate can be found using a similar approach to the one employed for the electrostatic potential of the conducting ellipsoid[67]. In ellipsoidal coordinates introduced in Sec. II-A [Eqs. (5), (6)], the solution for Ψ reads:

$$\Psi = -H_0 z\left(1 + A\frac{\gamma(\sigma)\sigma_s}{\gamma(\sigma_s)\sigma}\right), \tag{A-1a}$$

$$\gamma(\sigma) = \sigma\,\mathrm{acoth}\,\sigma - 1, \tag{A-1b}$$

$$A = -\chi\frac{\sigma_s(\sigma_s^{\,2}-1)}{1+\chi n_{\mathrm{II}}}, \tag{A-1c}$$

$$n_{\mathrm{II}} = (\sigma_s^{\,2}-1)\gamma(\sigma_s), \tag{A-1d}$$

recalling that $\sigma_s = a/c = a/\sqrt{a^2-b^2}$ is the value of σ on the aggregate surface. The components H_σ and H_τ of the magnetic field $\mathbf{H} = -\nabla\Psi$ outside the aggregate as well as its absolute value H can be calculated as:

$$H_\sigma = -\frac{1}{\sqrt{g_{\sigma\sigma}}}\frac{\partial\Psi}{\partial\sigma}, \qquad H_\tau = -\frac{1}{\sqrt{g_{\tau\tau}}}\frac{\partial\Psi}{\partial\tau}, \qquad H^2 = H_\sigma^{\,2} + H_\tau^{\,2} \tag{A-2}$$

where the metric coefficients $g_{\sigma\sigma}$ and $g_{\tau\tau}$ are given by Eq. (6).

The difference of the dimensionless energies $(u-u_0)$, intervening into the integral I appearing in Eq. (9), is given by the following expression:

$$u-u_0=\frac{U-U_0}{k_BT}=-\xi\Gamma(\sigma,\tau), \tag{A-3}$$

where the magnetic field parameter $\xi=-u_0$ is given by Eq. (10) and $\Gamma(\sigma,\tau)=H^2/H_0{}^2-1$. Combining Eqs. (A-1)-(A-2), after some algebra, we arrive at the following expression for the factor Γ, appearing in Eq. (A-3) for the energy difference of a particle around the aggregate as function of the particle position (σ,τ):

$$\Gamma(\sigma,\tau)=\frac{1}{\sigma^2-\tau^2}\left[\tau^2(\sigma^2-1)C(\sigma)+(1-\tau^2)D(\sigma)\right] \tag{A-4a}$$

$$C(\sigma)=2A\gamma'+A^2\gamma'^2 \tag{A-4b}$$

$$D(\sigma)=2A\sigma\gamma+A^2\gamma^2 \tag{A-4c}$$

$$\gamma'=\frac{d\gamma}{d\sigma}=\operatorname{acoth}\sigma-\frac{\sigma}{\sigma^2-1} \tag{A-4d}$$

Appendix B. Estimation of the integral *I* in Eq. (9)

We aim at expressing the integrals

$$I=\frac{1}{2}\int_{\sigma_S}^{\infty}\frac{d\sigma}{(\sigma^2-1)I_\sigma}, \tag{B-1a}$$

$$I_\sigma=\int_0^1 e^{-(u-u_0)}d\tau=\int_0^1 e^{\lambda\Gamma(\sigma,\tau)}d\tau \tag{B-1b}$$

as function of the magnetic field parameter ξ, the aggregate aspect ratio r_a and the aggregate susceptibility χ.

First, we obtain the following asymptotic values of I_σ and I at ξ=0 – the case when the magnetophoretic particle flux is neglected:

$$I_\sigma=1;\ I=\frac{1}{2}\operatorname{acoth}\sigma_s\approx\frac{1}{2}\ln(2r_a)\ \text{at}\ \lambda\to 0\ \text{and}\ r_a>>1; \tag{B-2}$$

At nonzero values of ξ and at the considered high aspect ratio limit $r_a>>1$, the integrand of I_σ exhibits a sharp increase close to the aggregate tips, i.e. at $\sigma\approx\sigma_s$ and in the vicinity of the integration limit $\tau=1$, while it takes a value close to unity on the rest of the integration interval. At such condition the term $\Gamma(\sigma,\tau)$ [Eq. (A-4)] can be expanded in Taylor series in the vicinity of the point $\tau=1$ and the integral I_σ can be evaluated as follows:

$$I_\sigma \approx \int_0^1 \exp\left[\xi\left(\Gamma(1)-\left(\frac{\partial\Gamma}{\partial\tau}\right)_{\tau=1}(1-\tau)\right)\right]d\tau \approx \frac{e^{\xi\Gamma(1)}}{\xi\left(\partial\Gamma/\partial\tau\right)_{\tau=1}} = \frac{(\sigma^2-1)e^{\xi C(\sigma)}}{2\xi(\sigma^2 C(\sigma)-D(\sigma))} \quad \text{(B-3)}$$

where the functions $C(\sigma)$ and $D(\sigma)$ are given by Eqs. (A-4b), (A-4c).

This evaluation is only valid at $\sigma \approx \sigma_s$ while at larger distances σ from the aggregate surface the integral falls to its asymptotic value of 1. Nevertheless Eq. (B-3) will allow obtaining an approximate analytical expression for the integral I. To this purpose, both numerical and analytical estimations of the integrand $1/\left[(\sigma^2-1)I_\sigma\right]$ of I are plotted in Fig. 12a as function of σ/σ_s for r_a=100, ξ=1 and χ=4.5. Analytical estimation (dashed curve) seems to be rather precise at $\sigma/\sigma_s < 1.00003$ as compared to the numerical result (solid curve). At $\sigma/\sigma_s > 1.00008$, the numerical estimation gives $I_\sigma \approx 1$ and the integrand is approximately equal to $1/(\sigma^2-1)$ as inferred from comparison between the dotted and the solid lines in Fig. 12a.

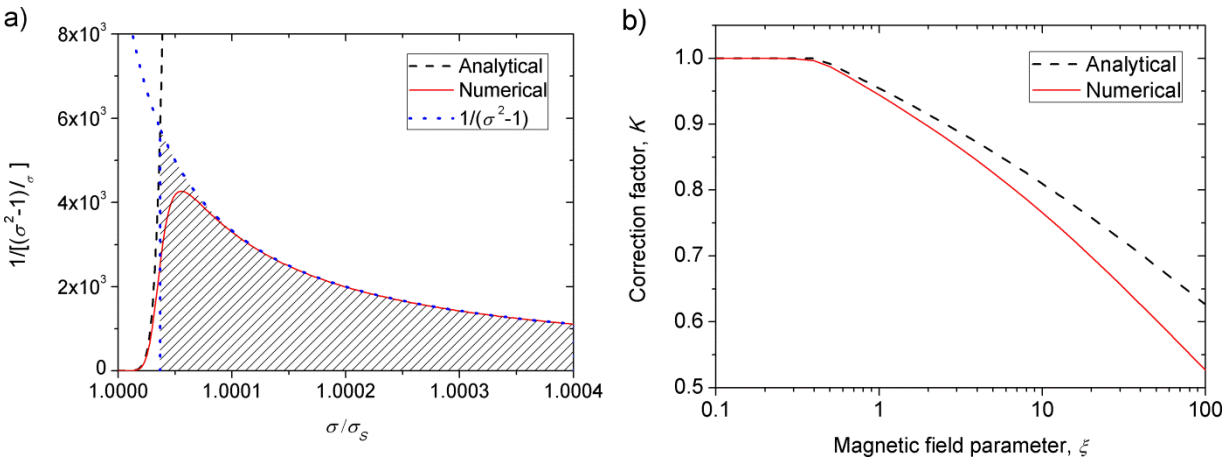

Fig. 12. The integrand of I as a function of σ/σ_s for ξ=1 (a); the correction factor K as a function of the magnetic field parameter ξ (b). Both figures (a) and (b) are plotted for r_a=100 and χ=4.5.

The exact value of the integral I represents the area below the dotted curve in Fig. 12a. This area can be roughly estimated as the area of the hatched figure whose upper border is defined by the curve $1/(\sigma^2-1)$ and the left border – by a vertical line corresponding to the intersection between the theoretical solid curve and $1/(\sigma^2-1)$ curve. This corresponds to the following approximate expression for I:

$$I \approx \frac{1}{2}\int_{\sigma_C}^{\infty}\frac{d\sigma}{\sigma^2-1} = \frac{1}{2}\operatorname{acoth}\sigma_C, \quad \text{(B-4)}$$

where σ_C is found from Eq. (B-3), in which I_σ is set to unity. The equation $I_\sigma(\sigma_C)=1$ has an approximate analytical solution in the limit r_a>>1 and gives the following explicit expression for the integral I:

$$I \approx \frac{1}{2}\ln\left[2r_a\left(\frac{\left(1+\delta/\xi\right)^{1/2}-1}{\chi}\right)^{1/2}\right] \qquad \text{(B-5a)}$$

$$\delta = \ln\left(2\chi(\chi+2)\xi r_a^{\,2}\right) \qquad \text{(B-5b)}$$

Finally the integral I can be presented as a product of its value at ξ=0 by a correction factor K defined as follows:

$$I \approx \frac{1}{2}K\ln(2r_a) \sim \frac{1}{2}K\ln r_a \text{ at } r_a >> 1, \qquad \text{(B-6a)}$$

$$K = \begin{cases} K^*, & K^* \le 1 \\ 1, & K^* > 1 \end{cases} \qquad K^* = 1 + \frac{1}{2}\frac{\ln\left[\left(\left(1+\delta/\xi\right)^{1/2}-1\right)/\chi\right]}{\ln(2r_a)} \qquad \text{(B-6b)}$$

where δ is given by Eq. (B-5b), and the conditional expression in Eq. (B-6b) is introduced in order to avoid the values of K>1 at low parameters ξ for which Eq. (B-3)-(B-5) are no longer valid but the value of K is close to unity. In the whole range of ξ, the correction factor K can be evaluated numerically as $K = 2I/\ln(2r_a)$, where I [Eq. (B-1)] is integrated numerically.

Both numerical and analytical values of the correction factor K are plotted as function of the magnetic field parameter ξ in Fig. 12b for r_a=100 and χ=4.5. Analytical and numerical calculations show a slow decrease of K as function of ξ, in agreement with a logarithmic decrease predicted by Eq. (B-6b). For instance, K decreases only by a factor of about 2 when ξ varies from 0 to 100. Such a small decrease could be explained by the fact that magnetic field in the vicinity of strongly elongated aggregates is everywhere close to the external field H_0, except for the aggregate tips; this leads to a rather weak magnetophoretic fluxes and results to a weak dependence of K on ξ. Finally, the relative error of the analytical estimate of K [Eq. (B-6b)] is less than 6% at ξ<10 and reaches 19% at ξ=100.

Appendix C. Estimation of the aggregate flux [Eq. (25)]

For evaluation of the integral in Eq. (24) for the aggregate flux, it is more convenient to use a spherical coordinate system (r, θ) introduced in Fig. 3. First, we have to express the magnitudes z and dz on the surface of the control ellipsoid, intervening into Eq. (24), through the angle θ:

$$z = r\cos\theta = \frac{\alpha\cos\theta}{\left(r_a^{\,2}\sin^2\theta + \cos^2\theta\right)^{1/2}}, \qquad \text{(C-1)}$$

$$dz = \frac{dz}{d\theta}d\theta = -\frac{\alpha r_a^{\,2}\sin\theta}{(r_a^{\,2}\sin^2\theta + \cos^2\theta)^{3/2}}d\theta\,. \qquad \text{(C-2)}$$

Using the last expressions along with the relationship $\alpha = 2a/\Phi^{1/3}$ in Eq. (24) and applying the limit r_a>>1, we arrive at the following approximate expression for the aggregate flux:

$$J \approx \frac{n\zeta_\perp \mu_0 M^2 V^2}{2a^2}\int_0^{\theta_0}\left[-2+(1+\psi\sin 2\theta+\psi^2\sin^2\theta)^{-3/2}+(1-\psi\sin 2\theta+\psi^2\sin^2\theta)^{-3/2}\right]\sin\theta d\theta =$$
$$= \frac{n\zeta_\perp \mu_0 M^2 V^2}{2a^2}\left[2\cos\theta_0 - \frac{\cos\theta_0-\psi\sin\theta_0}{\left(1-\psi\sin 2\theta_0+\psi^2\sin^2\theta_0\right)^{1/2}} - \frac{\cos\theta_0+\psi\sin\theta_0}{\left(1+\psi\sin 2\theta_0+\psi^2\sin^2\theta_0\right)^{1/2}}\right] \qquad \text{(C-3)}$$

where we denoted $\psi = r_a\Phi^{1/3}$ and the angle θ_0 corresponds to the position on the control ellipsoid surface [Fig. 3a] where the flux density is zero. This corresponds to the condition:

$$-2+(1+\psi\sin 2\theta_0+\psi^2\sin^2\theta_0)^{-3/2}+(1-\psi\sin 2\theta_0+\psi^2\sin^2\theta_0)^{-3/2}=0 \qquad \text{(C-4)}$$

Explicit solutions of Eq. (C-4) with respect to θ_0 exist only in the limits of small and high ψ giving the following asymptotes for the flux:

$$J = \begin{cases} \dfrac{4\Phi^{5/3}\mu_0 M^2}{25\sqrt{5}\eta_0}\ln r_a, & \psi = r_a\Phi^{1/3} << 1 \\ \dfrac{\Phi\mu_0 M^2}{6\eta_0}\dfrac{\ln r_a}{r_a^{\,2}}, & \psi = r_a\Phi^{1/3} >> 1 \end{cases} \qquad \text{(C-5)}$$

In deriving the last equation from Eq. (C-3), we have used $n = \Phi/V$ for the number fraction of aggregates and $\zeta_\perp \approx \left(\ln(2r_a)+1/2\right)/(8\pi\eta_0 a) \sim \ln r_a/(8\pi\eta_0 a)$ for the transverse component of the aggregate hydrodynamic mobility[77] at r_a>>1. Beyond these two asymptotes, using numerical solution for θ_0 in Eq. (C-3), we get a numerical result for the aggregate flux, which is fitted by Eq. (25) of Sec. II-B at a maximal error of 5.2% at $\psi \approx 1.5$.

References

[1] C. T. Yavuz, J.T. Mayo, W. W. Yu, A. Prakash, J. C. Falkner, S. Yean, L. Cong, H. J. Shipley, A. Kan, M. Tomson, D. Natelson, and V. L. Colvin, Science **314**, 964 (2006).

[2] R. D. Ambashta, and M. Sillanppa, J. Hazard. Mater., **180**, 38 (2010).

[3] A. Ito, M. Shinkai, H. Honda, and T. Kobayashi, J. Biosci. Bioeng. **100**, 1 (2005).

[4] C. Sun, J. S.H. Lee, and M. Zhang, Advanced Drug Delivery Reviews **60**, 1252 (2008).

[5] M. Zborowski and J. J. Chalmers, *Magnetic Cell Separation* (Elsevier, Amsterdam, 2008).

[6] C. Okoli, A. Fornara, J. Qin, M.S, Toprak, G. Dalhammar, M. Muhammed, and G. Rajarao, J. Nanosci. Nanotechnol. **11**, 1533 (2011).

[7] A. Ditsch, J. Yin, P.E. Laibinis, D.I.C Wang, and T.A. Hatton, Biotechnol. Prog. **22**, 1153 (2006).

[8] A. Jordan, R. Scholz, K. Maier-Hau, M. Johannsen, P. Wust, J. Nadobny, H. Schirra, H. Schmidt, S. Deger, S. Loening, W. Lanksch, and R. Felix, J. Magn. Magn. Mater. **225**, 118 (2001).

[9] R. Hergt, S. Dutz, R. Müller and M. Zeisberger, J. Phys.: Condens. Matter **18**, S2919 (2006).

[10] L. Douziech-Eyrolles, H. Marchais, Katel Hervé, E. Munnier, C. Linassier, P. Dubois, and I. Chourpa, Int. J. Nanomedicine **2**, 541 (2007).

[11] J. Esterlich, E. Escribano, J. Queralt and M.-A. Busquets, Int. J. Mol. Sci. **16**, 8070 (2015).

[12] M. N. Bouchlaka, G. D. Sckisel, D. Wilkins, E. Maverakis, A. M. Monjazeb, M. Fung, L. Welniak, D. Redelman, A. Fuchs, C. A. Everensel, and W. J. Murphy, PloS One **7**, e48049 (2012).

[13] Wang B., C. Bienvenu, J. Mendez-Garza, P. Lançon, A. Madeira, P. Vierling, Ch. Di Giorgio, and G. Bossis, J. Magn. Magn. Mater. **344**, 193 (2013).
[14] M. A. M. Gijs, F. Lacharme, and U. Lehmann, Chem. Rev. **110**, 1518 (2010).
[15] M. Mahoudi, M. Zhao, Y. Matsuura, S. Laurent, P. C. Yang, D. Bernstein, P. Ruiz-Lozano, and V. Serpooshan, BioImpacts **6**, 111 (2016).
[16] L. Rodriguez-Arco, I. A. Rodriguez, V. Carriel, A. B. Bonhome-Espinosa, F. Campos, P. Kuzhir, J.D.G. Duran, and M. T. Lopez-Lopez, Nanoscale **8**, 8138 (2016).
[17] G. De Las Cuevas, J.Faraudo, and J. Camacho, J. Phys. Chem. C **116**, 945 (2008).
[18] S. P. Yeap, P. Y. Toh, A. L. Ahmad, S. C. Low, S. A. Majetich and J. K. Lim, J. Phys. Chem. C **116**, 22561 (2012).
[19] J. S. Andreu, J. Camacho, J. Faraudo, M. Benelmekki, C. Rebollo, and L. M. Martínez , Phys. Rev. E **84**, 021402 (2011).
[20] K. Van Netten, J. Zhou, K. P. Galvin, and R. Moreno-Atanasio, Chem. Eng. Sci. **93**, 229 (2013).
[21] R.E. Rosensweig, *Ferrohydrodynamics* (Cambridge University Press, Cambridge, New York, 1985).
[22] M. Fermigier, and A. P Gast, J. Coll. Int. Sci. **154**, 522 (1992).
[23] J. H. E. Promislow, A. P. Gast and M. Fermigier, J. Chem. Phys. **102**, 5492 (1995).
[24] F. Martinez Pedrero, A. El-Harrak, J.C. Fernandez-Toledano, M. Tirado-Miranda, J.Baudry, A. Schmitt, J. Bibette and J. Callejas-Ferrnandez, Phys. Rev. E **78**, 011403 (2008).
[25] J. E. Martin, J. Odinek, and T. C. Halsey, Phys. Rev. Lett. **69**, 1524 (1992).
[26] A. S. Silva and D. Wirtz, Langmuir **14**, 578-581 (1998).
[27] M. Hagenbüchle and J. Liu, J. Appl. Optics **36**, 76664-7671 (1997).
[28] G. Bossis, C. Métayer and A. Zubarev, Phys. Rev. E **76**, 041401 (2007).
[29] G. Bossis, O. Volkova, S. Lacis, and A. Meunier, in *Magnetorheology: Fluids, Structures and Rheology*, edited by S. Odenbach (Springer, Berlin, 2002).
[30] J. H. E. Promislow and A. P. Gast, Phys. Rev. E **56,** 642 (1997).
[31] J. W. Swan, P. A. Vasquez, P. A. Whitson, E. M. Fincke, K. Wakata, S. H. Magnus, F. De Winne, M. R. Barratt, J. H. Agui, R. D. Green, N. R. Hall, D. Y. Bohman, Ch. T. Bunnell, A. P. Gast, and E. M. Furst, Proc. Natl. Acad. Sci. USA **109**, 16023 (2012).
[32] J. Faraudo, J. S. Andreu and J. Camacho, Soft Matter **9**, 6654 (2013).
[33] G. Bossis, P. Lançon, A. Meunier, L. Iskakova, V. Kostenko, and A. Zubarev, Physica A **392**, 1567 (2013).
[34] S. Miyazima, P. Meakin, and F. Family, Phys. Rev. A **36**, 1421 (1987).
[35] G. Bossis, L. Iskakova, V. Kostenko, and A. Zubarev, Physica A **390**, 2655-2663 (2011).
[36] H. See and M. Doi, J. Phys. Soc. Jpn. **60**, 2778 (1991).
[37] A. O. Tsebers, Magn. Gidrodin. **18**, 42 (1982) [Magnetohydrodynamics **18**, 137 (1982)].
[38] Yu. A. Buyevich, and A. O. Ivanov, Physica A **190**, 276 (1992).
[39] J. Liu, E. M. Lawrence, A. Wu, M. L. Ivey, G. A. Flores, K. Javier, J. Bibette, and J. Richard, Phys. Rev. Lett. **74**, 2828 (1995).
[40] C-Y Hong, I.J. Jang, H.E. Horng, C.J.Hsu Y. D.Yao, H.C. Yang, J. Appl. Phys. **81**, 4275-4277 (1997).
[41] A.Y. Zubarev and Iskakova, L.Y. Phys. Rev. E **65**, 061406 (2002).
[42] A. P. Hynninen and M. Dijkstra, Phys. Rev. Lett. **94**, 138303 (2005).
[43] E. Dubois , R. Perzynski , F. Boué , and V. Cabuil, *Langmuir* **16**, 5617–5625 (2000).
[44] F. Cousin, E. Dubois and V. Cabuil, J. Chem. Phys. **115**, 6051 (2001).
[45] F. Cousin, E. Dubois, and V. Cabuil, Phys. Rev. E **68**, 021405 (2003).
[46] T. A. Prokopieva, V. A. Danilov, S. S. Kantorvich, and C. Holm, Phys. Rev. E **80**, 031404 (2009).
[47] C. Holm, and J. J. Weiss, Current Opinion Coll. Int. Sci. **10**, 031404 (2005).
[48] V. Socoliuc, and D. Bica, Prog. Coll. Polym. Sci. **117**, 131 (2001).
[49] J. M. Laskar, J. Philip, and B. Raj, Phys. Rev. E **82**, 021402 (2010).
[50] A. Yu. Zubarev, and A. O. Ivanov, Phys. Rev. E. **55**, 7192 (1997).
[51] A. O. Ivanov, and A.Yu. Zubarev, Phys. Rev. E **58**, 7517 (1998).
[52] A. Ditsch, S. Lindenmann, P.E. Laibinis, D.I.C. Wang, and T.A. Hatton, Ind. Eng. Chem. Res. **44**, 6824 (2005).
[53] B. Frka-Petesic, J Fresnais, JF Berret, V Dupuis, R Perzynski, and O Sandre, J.Magn. Magn. Mater. **321**, 667-670 (2009).
[54] V. Socoliuc, L. Vékas, and R. Turcu, Soft Matter **9**, 3098 (2013).
[55] C. Magnet, P. Kuzhir, G. Bossis, A. Meunier, L. Suloeva, and A. Zubarev, Phys. Rev. E **86**, 011404 (2012).

[56] V. Torrisi, A. Graillot, L. Vitorazi, Q. Crouzet, G. Marletta, C. Loubat, and Berret J.-F., Biomacromolecules **15**, 3171 (2014).
[57] C. Magnet, P. Kuzhir, G. Bossis, A. Meunier, S. Nave, A. Zubarev, C. Lomenech and V. Bashtovoi, Phys. Rev. E **89**, 032310 (2014).
[58] A. S. Ivanov and A. F. Pshenichnikov, Phys. Fluids **26**, 012002 (2014).
[59] C. Magnet, M. Akouala, P. Kuzhir, G. Bossis, A. Zubarev, and N.M. Wereley, J. Appl. Phys. **117**; 17C719 (2015).
[60] G. Orlandi, P. Kuzhir, Y. Izmaylov, J. Alves Marins, H. Ezzaier, L. Robert, F. Doutre, X.Noblin, C.Lomenech, G.Bossis, A. Meunier, G.Sandoz and A. Zubarev, Phys. Rev. E **93**, 062604 (2016).
[61] P. Kuzhir, C, Magnet, H, Ezzaier, A. Zubarev, and G. Bossis, J. Magn. Magn. Mater. *In press*.
[62] L. D landau and E. M. Lifshitz, *Physical kinetics* (Pergamon, Oxford, 1981).
[63] J.C. Bacri, and D. Salin, J Magn. Magn. Mater **39**, 48 (1983).
[64] F. Pshenichnikov, and I. Yu. Shurubor, Bull. Acad. Sci. USSR, Phys. Ser. **51**, 40 (1987).
[65] J.C. Bacri, R. Perzynski, D. Salin, V. Cabuil, and R. Massart, J. Coll. Int. Sci. **132**, 43 (1989).
[66] V. G. Levich, *Physico-Chemical Hydrodynamics* (Prentice-Hall, Englewood Cliffs. N.J., 1962).
[67] L. D. Landau, and E.M. Lifshitz, *Electrodynamics of Continuous Media* (Pergamon, New York, 1984).
[68] G. Korn, and T. Korn, *Mathematical handbook for Scientists and Engineers* (McGraw-Hill New York, 1961).
[69] A. Zubarev, L. Iskakova, M. T. Lopez-Lopez, P. Kuzhir and G. Bossis, J. Rheol. **58**, 1673 (2014).
[70] R.M. Christensen, *Mechanics of Composite Materials*, Krieger Publishing Company, Malabar (1979).
[71] S. Berthier, *Optique des milieux composites*, Polytechnica, Paris (1993).
[72] D. Bica, L. Vekas, M. V. Avdeev, O. Marinica, V. M. Socoliuc, M. Balasoiu and V. M. Garamus, J. Magn. Magn. Mater. **311**, 17 (2007).
[73] W. B. Russell, D. A. Saville, and W. R. Schowalter, *Colloidal Dispersions* (Cambridge University Press, Cambridge, 1989)
[74] K. Erglis, A.Tatulcenkov, G.Kienbergs, O.Petrichenko, F. G. Ergin, B. B. Watz and A. Cēbers, J Fluid. Mech. **714**, 612-633 (2013).
[75] A.O. Ivanov, Kolloidnyi. Zhurnal. **57**, 347 (1995).
[76] A. O. Ivanov and E. V. Novak, Colloid J. **69**, 302–311 (2007).
[77] H. Brenner, Int. J. Multiphase Flow **1**, 195-341 (1974).